



ATLAS NOTE

ATLAS-CONF-2016-076

4th August 2016



Search for direct top squark pair production and dark matter production in final states with two leptons in $\sqrt{s} = 13$ TeV pp collisions using 13.3 fb^{-1} of ATLAS data

The ATLAS Collaboration

Abstract

The results of a search for new phenomena in events with two leptons (electrons or muons) are reported, using 13.3 fb^{-1} of integrated luminosity from LHC pp collisions at $\sqrt{s} = 13$ TeV collected by the ATLAS detector. Three possible signals are targeted by dedicated selections: the pair production of top squarks decaying via the three body mode $\tilde{t}_1 \rightarrow \tilde{\chi}_1^0 W b$; the pair production of top squarks decaying via $\tilde{t}_1 \rightarrow \tilde{\chi}_1^\pm b \rightarrow \tilde{\chi}_1^0 W^{(*)} b$; and the production of dark matter in association with a $t\bar{t}$ pair. No excess above the Standard Model expectation is observed, and exclusion limits at 95% confidence level are derived for the different models.

1 Introduction

The Standard Model (SM) of particle physics is believed to be the low energy limit of a more general theory. Many arguments point to the need to extend the SM, among them the need to stabilise the Higgs mass against radiative corrections from Planck scale physics and the need to explain the nature of dark matter (DM) [1–4]. Both these shortcomings might be addressed by new physics at the TeV scale and motivate many of the new particle searches at the LHC.

One of the most compelling theories beyond the SM is Supersymmetry (SUSY) [5–10]. SUSY is a spacetime symmetry that postulates for each Standard Model (SM) particle the existence of a partner particle whose spin differs by one-half unit. The introduction of gauge-invariant and renormalisable interactions into SUSY models can violate the conservation of baryon number (B) and lepton number (L), resulting in a proton lifetime shorter than current experimental limits [11]. This is usually solved by assuming that the multiplicative quantum number R -parity [12], defined as $R = (-1)^{3(B-L)+2S}$, is conserved.

In the framework of a generic R -parity-conserving Minimal Supersymmetric Standard Model (MSSM) [13, 14], SUSY particles are produced in pairs, and the lightest supersymmetric particle (LSP) is stable and a candidate for dark matter [15, 16]. The scalar partners of right-handed and left-handed quarks (squarks), \tilde{q}_R and \tilde{q}_L , can mix to form two mass eigenstates, \tilde{q}_1 and \tilde{q}_2 , with \tilde{q}_1 defined to be the lighter one. In the case of the supersymmetric partner of the top quark \tilde{t} , large mixing effects and small on-diagonal terms can lead to one top squark mass eigenstate, \tilde{t}_1 , that is significantly lighter than the other squarks. The charginos and neutralinos are mixtures of the bino, winos and higgsinos that are superpartners of the U(1), SU(2) gauge bosons and the Higgs bosons, respectively. Their mass eigenstates are referred to as $\tilde{\chi}_i^\pm$ ($i = 1, 2$) and $\tilde{\chi}_j^0$ ($j = 1, 2, 3, 4$) in the order of increasing masses. In a large variety of models, the LSP is the lightest neutralino $\tilde{\chi}_1^0$.

One of the best motivated candidates for a DM particle is a weakly interacting massive particle (WIMP) [17]. At the Large Hadron Collider (LHC), one can search for DM particles (χ) produced in pp collisions. As they are weakly interacting, they escape the detectors, leading to a momentum imbalance of the event in the transverse plane. Searches for DM associated production with heavy quarks have been presented by ATLAS [18] and CMS [19–21], using Effective Field Theories (EFT) [22–24] to model the DM signals. Instead, this search is focused on simplified models of DM production which involve spin-0 mediators to the dark sector [25–27] thus avoiding the limitations of the EFT approach at colliders [28–30]. These models are one of the simplest UV complete extensions of the effective field theory approach to dark matter, which involves the addition of a spin-0 mediator between the DM and SM sectors. Two choices for DM simplified models are considered: one where the interaction with the SM is mediated by a scalar (φ), and the second with only a light pseudoscalar (a) mediator (assuming that the associated scalar is decoupled from the low-energy spectrum). Following the notation of Ref. [17], the model has four parameters: the masses of the mediator and the DM particle, the DM-mediator coupling (g_χ), and the universal SM-mediator coupling (g_q). In this note, the assumption $g_q = g_\chi = g$ is made.

In order to fulfil precision constraints from flavour measurements, these models assume Yukawa-like couplings between the dark sector mediator and the SM fermions. This motivates the choice of studying these models in heavy flavour quark final states. Couplings to top quarks are considered in this search.

In this document a search for new physics is reported, using 13.3 fb^{-1} of proton-proton collision data collected by the ATLAS experiment in 2015 and 2016. The final state of interest includes two isolated

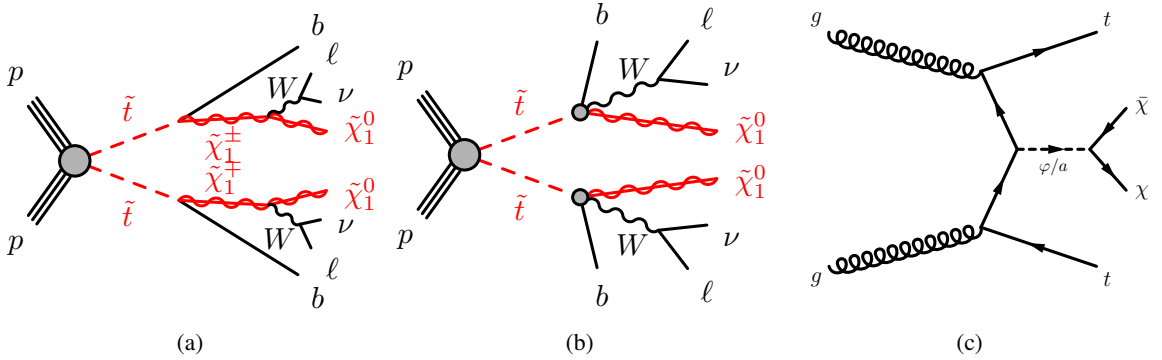


Figure 1: Diagrams representing the three main signals targeted by the analyses: (a) the decay of a top squark via chargino which is targeted by the hadronic m_{T2} search, (b) the 3-body decay mode of a top squark and (c) the production of dark matter particles in association with a $t\bar{t}$ pair.

electrons or muons and missing transverse momentum. Three different selections, here referred as to “hadronic m_{T2} ”, “three-body” and “dark matter”, are considered. The first targets the pair production of top squarks, each of them decaying through the three-body mode into $bW\tilde{\chi}_1^0$. This is expected to be the dominant mode when $m(\tilde{\chi}_1^0) + m(W) + m(b) < m(\tilde{t}_1) < m(\tilde{\chi}_1^0) + m(t)$ and the stop is lighter than the lightest chargino $\tilde{\chi}_1^\pm$. Results are interpreted in the $(m(\tilde{\chi}_1^0), m(\tilde{t}_1))$ plane. The second set of selections targets the decay mode to the lightest chargino and a b quark, followed by the chargino decay into the lightest neutralino, a lepton and a neutrino. The results are interpreted in the $(m(\tilde{\chi}_1^0), m(\tilde{t}_1))$ plane, assuming a 100% branching ratio for the decay mode considered, and a chargino mass either equal to 106 GeV or to twice the lightest neutralino mass. The third set of selections targets the production of DM in association with a leptonically decaying $t\bar{t}$ pair. Results are interpreted in the plane formed by the mediator mass and the Dark Matter particle mass, assuming either a scalar or pseudoscalar mediator. Mass limits for a fixed $g=3.5$ coupling and coupling limits for a fixed mass are provided. Diagrams for the different signal processes are presented in Fig. 1. Previous ATLAS [31, 32] and CMS [33–39] analyses have placed exclusion limits at 95% confidence level (CL) on the signal scenarios considered here.

2 ATLAS detector

The ATLAS detector [40] at the LHC is a multi-purpose particle detector with a forward-backward symmetric cylindrical geometry and it covers nearly the entire solid angle around the collision point.¹ It consists of an inner tracking detector surrounded by a thin superconducting solenoid, electromagnetic and hadron calorimeters, and a muon spectrometer incorporating three large superconducting toroid magnets. The inner-detector system (ID) is immersed in a 2 T axial magnetic field and provides charged particle tracking in the range $|\eta| < 2.5$. It consists of a high-granularity silicon pixel detector, which covers the vertex region and typically provides three measurements per track, a silicon microstrip tracker, which usually provides four two-dimensional measurement points per track, and a transition radiation

¹ ATLAS uses a right-handed coordinate system with its origin at the nominal interaction point (IP) in the centre of the detector and the z -axis along the beam pipe. The x -axis points from the IP to the centre of the LHC ring, and the y -axis points upwards. Cylindrical coordinates (r, ϕ) are used in the transverse plane, ϕ being the azimuthal angle around the z -axis. The pseudorapidity is defined in terms of the polar angle θ as $\eta = -\ln \tan(\theta/2)$.

tracker, which enables radially extended track reconstruction up to $|\eta| = 2.0$. The transition radiation tracker also provides electron identification information based on the fraction of hits (typically 30 in total) above a higher energy deposit threshold corresponding to transition radiation. During the first LHC long shutdown, a new pixel layer, known as Insertable B-Layer (IBL) [41], was added at a radius of 33 mm. The calorimeter system covers the pseudorapidity range $|\eta| < 4.9$. Within the region $|\eta| < 3.2$, electromagnetic calorimetry is provided by barrel and endcap high-granularity lead/liquid-argon (LAr) electromagnetic sampling calorimeters with an accordion geometry, with an additional thin LAr presampler covering $|\eta| < 1.8$, to correct for energy loss in material upstream of the calorimeters. Hadronic calorimetry is provided by an iron/scintillating-tile sampling calorimeter, segmented into three barrel structures within $|\eta| < 1.7$, and two copper/LAr hadronic endcap calorimeters. The solid angle coverage is completed with forward copper/LAr and tungsten/LAr calorimeter modules optimised for electromagnetic and hadronic measurements respectively. The Muon Spectrometer (MS) comprises separate trigger and high-precision tracking chambers measuring the deflection of muons in a magnetic field generated by superconducting air-core toroids. The precision chamber system covers the region $|\eta| < 2.7$ with three layers of monitored drift tubes, complemented by cathode strip chambers in the forward region, where the background is higher. The muon trigger system covers the range $|\eta| < 2.4$ with resistive plate chambers in the barrel, and thin gap chambers in the endcap regions. A two-level trigger system is used to select events [42]. There is a low-level hardware trigger implemented in custom electronics, which reduces the incoming data rate to a design value of ~ 100 kHz using a subset of detector information, and a high-level software trigger which selects interesting final state events with software algorithms accessing the full detector information.

3 Physics object selection

Data were collected by the ATLAS detector in 2015 and 2016 during pp collisions at a centre-of-mass energy of $\sqrt{s} = 13$ TeV, with a peak instantaneous luminosity of $\mathcal{L} = 1.0 \times 10^{34} \text{ cm}^{-2}\text{s}^{-1}$, a bunch spacing of 25 ns, and an average number of additional pp interactions per bunch crossing (pileup) of $\langle\mu\rangle = 14$ in 2015 and $\langle\mu\rangle = 21$ in 2016. Only events taken in stable beam conditions, and in which the trigger system, the tracking devices and the calorimeters were operational, are considered in this analysis. After data-quality requirements, the data sample amounts to an integrated luminosity of 13.3 fb^{-1} with an uncertainty of $\pm 2.9\%$. This preliminary uncertainty is derived, following a methodology similar to that detailed in Refs. [43] and [44], from a preliminary calibration of the luminosity scale using x-y beam-separation scans performed in August 2015 and May 2016.

Candidate events are required to have a reconstructed vertex with at least two associated tracks with $p_T > 400$ MeV. The vertex with the highest scalar sum of the squared transverse momenta of the associated tracks is considered the primary vertex of the event.

Electron candidates are reconstructed from an electromagnetic calorimeter energy depositions matched to ID tracks and are required to have $|\eta| < 2.47$, a transverse momentum $p_T > 7$ GeV, and to pass a loose likelihood-based identification requirement [45, 46]. The likelihood input variables include measurements of calorimeter shower shapes and of track properties from the ID.

Muon candidates are reconstructed in the region $|\eta| < 2.5$ from muon spectrometer tracks matching ID tracks. Candidate muons must have $p_T > 5$ GeV and must pass the medium identification requirements defined in Ref. [47], based on requests on the number of hits in the different ID and muon spectrometer subsystems, and on the significance of the charge to momentum ratio q/p [47].

Jets are reconstructed from three-dimensional energy clusters in the calorimeter [48] with the anti- k_t jet clustering algorithm [49] with a radius parameter $R = 0.4$. Only jet candidates with $p_T > 20 \text{ GeV}$ and $|\eta| < 2.8$ are considered as selected jets in the analysis. Jets are calibrated as described in Ref. [50]. In order to reduce the effects of pileup, for jets with $p_T < 60 \text{ GeV}$ and $|\eta| < 2.4$ a significant fraction of the tracks associated with each jet must have an origin compatible with the primary vertex, as defined by the jet vertex tagger [51]. Furthermore, for all jets the expected average energy contribution from pileup clusters is subtracted according to the jet area [50]. Jets resulting from b -quarks (called b -jets) are identified using the MV2c10 b -tagging algorithm, which is based on quantities such as impact parameters of associated tracks and reconstructed secondary vertices [52, 53]. This algorithm is used at a working point that provides 77% b -tagging efficiency in simulated $t\bar{t}$ events, and a rejection factor of about 134 for light-quark flavours and gluons and about 6 for charm jets.

To resolve reconstruction ambiguities, electron candidates sharing an inner detector track with a muon candidate are removed. Then, jet candidates within $\Delta R = \sqrt{\Delta y^2 + \Delta \phi^2} < 0.2$ (where y stands for the rapidity) from an electron candidate are removed, and the same is done for jets with fewer than three tracks which lie within $\Delta R < 0.4$ around a muon candidate. Finally, any lepton candidate within $\Delta R < 0.4$ from the centre of a surviving jet candidate is removed, in order to reject leptons from the decay of a b or c hadron.

Signal electrons must satisfy a medium likelihood-based identification requirement [45, 46] and the track associated with the electron must have a significance of the transverse impact parameter with respect to the reconstructed primary vertex, d_0 , of $|d_0|/\sigma(d_0) < 5$, with $\sigma(d_0)$ being the uncertainty on d_0 . Signal muons must have a $|d_0|/\sigma(d_0) < 3$. The tracks associated to the signal leptons must have a longitudinal impact parameter with respect to the reconstructed primary vertex, z_0 , satisfying $|z_0 \sin \theta| < 0.5 \text{ mm}$. Leptons are required to be isolated from other activity using a relatively loose p_T -based track- and calorimeter-based criteria designed to pass 99% of leptons from Z decays.

The E_T^{miss} is defined as the magnitude of the two-vector $\mathbf{p}_T^{\text{miss}}$ which is the negative vector sum of the transverse momenta of all identified physics objects (electrons, photons, muons, jets) and an additional soft term. The soft term is constructed from all tracks that are not associated with any physics object, and which are associated with the primary vertex. In this way, the E_T^{miss} is adjusted for the best calibration of the jets and the other identified physics objects above, while maintaining pileup independence in the soft term [54, 55].

4 Event selection

Events are accepted if they pass an online selection (trigger) requiring either two electrons, two muons or an electron and a muon. The trigger-level requirements on the leading and sub-leading lepton p_T are looser than those applied offline to ensure that trigger efficiencies are constant in the relevant phase space. The offline selection requires that the leading lepton has a p_T larger than 25 GeV and the subleading lepton a p_T larger than 20 GeV. In addition to the leptonic triggers, the “hadronic m_{T2} ” selection (see below) also accepts events passing an E_T^{miss} based trigger and having offline $E_T^{\text{miss}} > 200 \text{ GeV}$, in order to recover acceptance in events with soft lepton momenta (for events passing the E_T^{miss} trigger selection, the requirement on both lepton p_T is lowered to 10 GeV). In all cases, events are required to have exactly two oppositely charged signal leptons (electrons, muons, or one of each) with the invariant mass of these two objects, $m_{\ell\ell}$, being greater than 20 GeV (regardless of the flavours of the leptons in the pair), in order to remove leptons from low mass resonances. Simulated events are corrected to account for minor

differences in the signal lepton trigger, reconstruction and identification efficiencies between data and simulation.

4.1 Discriminators and Kinematic Variables

Different discriminators and kinematic variables are used in the analyses to separate the signal from the SM background.

The three-body search uses a number of “super-razor” variables that are defined in [56]. They are designed to identify events with two massive parent particles (i.e. top-squarks) that each decay into a set of visible (i.e. leptons) and invisible particles (i.e. neutrinos and neutralinos). These variables are:

- R_{pT} : The quantity R_{pT} is defined as:

$$R_{pT} = \frac{|\vec{J}_T|}{|\vec{J}_T| + \sqrt{\hat{s}_R}/4} \quad (1)$$

where \vec{J}_T is the vector sum of the momenta of all visible particles and the missing transverse momentum, and $\sqrt{\hat{s}_R}$ is the approximate centre of mass energy in the razor frame R (the pair production centre-of-mass frame). Since only the leptons are considered in the visible system the $|\vec{J}_T|$ will be over-estimated in events with additional activity, i.e. signal and top-quark production, which biases R_{pT} towards unity and provides rejection power against diboson production which tends towards zero.

- $1/\gamma_{R+1}$: This quantity is the inverse of the Lorentz factor, γ_{R+1} , associated with the boosts from the razor frame R to the approximations of the two decay frames of the parent particles. It is a measure of how the two visible systems are distributed, tending towards unity when visible particles are equal in momenta and collinear, while preferring lower values when they are back-to-back or having different momenta. It is observed to provide rejection power against both top-quark and diboson production processes.

- M_Δ^R : The quantity M_Δ^R is defined as:

$$M_\Delta^R = \frac{\sqrt{\hat{s}_R}}{\gamma_{R+1}} \quad (2)$$

This variable has a kinematic end-point that is proportional to the mass-splitting between the parent particle and the invisible particle. Therefore, it provides rejection against both top-quark and diboson production processes when it is required to be greater than the pole-mass of the W -boson, in which regime it also helps to reject the residual $Z/\gamma^* + \text{jets}$ background.

- $\Delta\phi_\beta^R$: The azimuthal angle between the razor boost from the laboratory to the R frame and the sum of the visible momenta as evaluated in the R frame. For systems where the invisible particle has a mass that is comparable to the pair-produced massive particle, this variable has a pronounced peak near π , making it, in general, a good discriminator in searches in a compressed spectra scenario.

Other kinematic variables considered in some of the analyses include:

- m_{T2}^{ll} and m_{T2}^{bb} : lepton-based and jet-based transverse mass. The transverse mass [57, 58] is a kinematic variable used to bound the masses of an unseen pair of particles which are presumed to have decayed semi-invisibly into particles which were seen. This quantity is defined as

$$m_{T2}(\mathbf{p}_{T,1}, \mathbf{p}_{T,2}, \mathbf{q}_T) = \min_{\mathbf{q}_{T,1} + \mathbf{q}_{T,2} = \mathbf{q}_T} \{ \max[m_T(\mathbf{p}_{T,1}, \mathbf{q}_{T,1}), m_T(\mathbf{p}_{T,2}, \mathbf{q}_{T,2})] \},$$

where m_T indicates the transverse mass,² $\mathbf{p}_{T,1}$ and $\mathbf{p}_{T,2}$ are the transverse momentum vectors of two particles (assumed to be massless), and $\mathbf{q}_{T,1}$ and $\mathbf{q}_{T,2}$ are vectors with $\mathbf{q}_T = \mathbf{q}_{T,1} + \mathbf{q}_{T,2}$. The minimisation is performed over all the possible decompositions of \mathbf{q}_T . For $t\bar{t}$ or WW decays, if the transverse momenta of the two leptons in each event are taken as $\mathbf{p}_{T,1}$ and $\mathbf{p}_{T,2}$, and E_T^{miss} as \mathbf{q}_T , $m_{T2}(\ell, \ell, E_T^{\text{miss}})$ is bounded sharply from above by the mass of the W boson [59, 60]. In the $\tilde{t}_1 \rightarrow b + \tilde{\chi}_1^\pm$ decay mode the upper bound is strongly correlated with the mass difference between the chargino and the lightest neutralino. If the transverse momenta of the two reconstructed b -jets in the event are taken as $\mathbf{p}_{T,1}$ and $\mathbf{p}_{T,2}$, and the lepton transverse momenta are added vectorially to the missing transverse momentum in the event to form \mathbf{q}_T , the resulting $m_{T2}(b, b, \ell + \ell + E_T^{\text{miss}})$ has a very different kinematic limit: for top-quark pair production it is approximately bounded by the mass of the top quark, whilst for top-squark decays the bound is strongly correlated to the mass difference between the top squark and the chargino. In this paper, $m_{T2}(\ell, \ell, E_T^{\text{miss}})$ is referred to simply as m_{T2}^{ll} , whilst $m_{T2}(b, b, \ell + \ell + E_T^{\text{miss}})$ is referred to as m_{T2}^{bb} .

- A variable called $E_{T,\text{min}}^{\text{bl}}$ is obtained by considering the four possible pairs of a b -jet and a lepton that can be constructed from two b -jets and two leptons, and taking the smallest value of $E^2 - p_z^2$ of these pairs.
- $\Delta\phi_{\text{boost}}$ and $\mathbf{p}_{\text{Tboost}}^{\ell\ell}$: the azimuthal angular distance between the $\mathbf{p}_T^{\text{miss}}$ vector and the $\mathbf{p}_{\text{Tboost}}^{\ell\ell} = \mathbf{p}_T^{\text{miss}} + \mathbf{p}_T^{\ell_1} + \mathbf{p}_T^{\ell_2}$ vector. The $\mathbf{p}_{\text{Tboost}}^{\ell\ell}$ variable, with magnitude $p_{\text{Tboost}}^{\ell\ell}$, is the opposite of the vector sum of all the transverse hadronic activity in the event.
- m_{eff} : the scalar sum of the E_T^{miss} , the transverse momenta of the two leptons and that of the two jets with the largest p_T in each event.
- $\cos\theta_b$: The cosine of the angle between the direction of motion of one of the two leptons and the beam axis in the centre-of-mass frame of the two visible leptons [61]. This variable is sensitive to the spin of the pair-produced particle, providing additional rejection against diboson backgrounds.

4.2 Hadronic m_{T2} selection

This search targets the process illustrated by Fig. 1a, and scenarios with a large mass difference between the top squark and the lightest chargino. When this difference is larger than the top quark mass, the values assumed by m_{T2}^{bb} for signal extend beyond the kinematic endpoint for $t\bar{t}$, which is the main background after the requirement of two leptons and two b -tagged jets. The event selection is based on such observation.

If the mass difference between the chargino and the neutralino is small, the transverse momentum of the two leptons can be small. Therefore, the selection makes use of a combination of E_T^{miss} -based and lepton-based triggers to maximise the signal acceptance. Events passing the E_T^{miss} trigger are required

² The transverse mass is defined by the equation $m_T = \sqrt{2|\mathbf{p}_{T,1}||\mathbf{p}_{T,2}|(1 - \cos(\Delta\phi))}$, where $\Delta\phi$ is the angle between the particles with transverse momenta $\mathbf{p}_{T,1}$ and $\mathbf{p}_{T,2}$ in the plane perpendicular to the beam axis.

to have both leptons with $p_T > 10$ GeV. Events selected by the dilepton trigger are still required to have $E_T^{\text{miss}} > 100$ GeV to improve the signal sensitivity.

In the same-flavour channels (ee and $\mu\mu$), the invariant mass of the two leptons is required to be outside the 71-111 GeV window. In order to make use of the $m_{T_2}^{bb}$ potential and its end-point at the top mass in top-quark pair production, the events are required to have exactly two identified b -jets in the final state.

Two signal regions (SR) are defined: $\text{SR}_{\text{Low}}^{\text{hadMT2}}$, optimised for $m(\tilde{t}) = 400$ GeV, and $\text{SR}_{\text{High}}^{\text{hadMT2}}$, suitable for a higher \tilde{t} mass. In both cases, samples of signal simulated events with a chargino mass of 100 GeV and a neutralino mass between 1 and 75 GeV have been used to find the optimal selection. The following selection is applied for the SRs:

- $m_{T_2}^{bb}$ is required to be larger than 220 GeV. As described in Section 4.1, this variable is expected to have a value smaller than the top quark mass in $t\bar{t}$ events while it extends to larger values for signal events. This selection thus removes most of the $t\bar{t}$ events, with the majority of events passing the selection have mistagged b -jets, a b -jet from an ISR gluon splitting rather than from the top decay, or mismeasured E_T^{miss} . The selection is less effective against the Wt backgrounds, for which one of the b -jets has to be from gluon splitting or a mistagged jet.
- The p_T of the leading lepton, $p_T^{\text{lept}1}$, is required to be smaller than 120 GeV. This selection exploits the fact that the leptons have a softer p_T spectrum in the expected signal compared to that of the top backgrounds.
- For $\text{SR}_{\text{High}}^{\text{hadMT2}}$, $E_{T,\text{min}}^{\text{bl}}$ is required to be larger than 180 GeV, this being the only difference between the two SR.

The selections applied to each SR are summarised in Table 1.

Table 1: Definition of the signal regions used in the hadronic m_{T_2} analysis. An horizontal dash indicates that no selection is applied. The trigger, trigger-related lower cuts on the lepton p_T and E_T^{miss} , and the lepton invariant mass cuts described in the text are applied for all regions. The criteria on $|m_{\ell\ell} - m_Z|$ are applied only to same-flavour events.

Variable	$\text{SR}_{\text{Low}}^{\text{hadMT2}}$	$\text{SR}_{\text{High}}^{\text{hadMT2}}$
$ m_{\ell\ell} - m_Z $ [GeV] (SF only)	>20	>20
b -jet multiplicity	2	2
$m_{T_2}^{bb}$ [GeV]	>220	>220
$p_T^{\text{lept}1}$ [GeV]	<120	<120
$E_{T,\text{min}}^{\text{bl}}$ [GeV]	-	>180

4.3 Three-body selection

The selection described here targets the three-body decay mode of the top squark (Fig. 1b) which, as already mentioned, is expected to be the dominant decay mode when the two-body decay modes into the lightest chargino and neutralino are kinematically forbidden, which occurs for $m(\tilde{t}_1) < m(\tilde{\chi}_1^\pm) + m(b)$ and $m(\tilde{t}_1) < m(\tilde{\chi}_1^0) + m(t)$.

In the same-flavour (SF) channels, the invariant mass $m_{\ell\ell}$ of the two-lepton system is required to be outside of the 81–101 window³. No requirement is applied on the different-flavour (DF) channels instead.

Two orthogonal signal regions, $\text{SR}_W^{\text{3-body}}$ and $\text{SR}_t^{\text{3-body}}$, are defined as summarised in Table 2. Both regions make use of a common set of requirements on R_{p_T} , $1/\gamma_{R+1}$, and in the two-dimensional $(\cos \theta_b, \Delta\phi_\beta^R)$ plane, to reject background while retaining as much signal as possible regardless of the exact stop decay topology. In addition, $\text{SR}_W^{\text{3-body}}$ requires exactly zero b -jets and $M_\Delta^R > 95 \text{ GeV}$. It targets the region where $\Delta m(\tilde{t}, \tilde{\chi}_1^0) \sim m_W$ by exploiting the fact that in such a scenario the b -jets in the stop decay chain have soft p_T spectra and hence are often not reconstructed. The large M_Δ^R requirement suppresses the top-quark and diboson production processes and enhances the signal sensitivity. A requirement of at least one b -jet and $M_\Delta^R > 110 \text{ GeV}$ is instead applied in $\text{SR}_t^{\text{3-body}}$. It targets the region where $\Delta m(\tilde{t}, \tilde{\chi}_1^0) \sim m_t$ by selecting b -jets. This requirement allows it to be disjoint to $\text{SR}_W^{\text{3-body}}$ but a slightly tighter M_Δ^R requirement is necessary to eliminate the additional background that originates from top-quark production processes.

Table 2: Signal region definitions for the three-body search. The trigger, trigger-related cuts on lepton p_T , and invariant mass cuts described in the text are always applied. The criteria on $|m_{\ell\ell} - m_Z|$ are applied only to same-flavour events.

Common selection		
Lepton flavour	SF, DF	
$ m_{\ell\ell} - m_Z \text{ [GeV]} \text{ (SF only)}$	> 10	
R_{p_T}	> 0.5	
$1/\gamma_{R+1}$	> 0.8	
$\Delta\phi_\beta^R$	$> 0.85 \cos \theta_b + 1.8$	
Region specific		
	$\text{SR}_W^{\text{3-body}}$	$\text{SR}_t^{\text{3-body}}$
b -jet multiplicity	$= 0$	> 0
$M_\Delta^R \text{ [GeV]}$	> 95	> 110

4.4 Dark Matter Selection

The search for dark matter targets the process shown in Fig. 1c. Since this produces two top quarks and two invisible particles, the final state contains the same objects of the signals targeted by the other searches when the W bosons produced by both top quarks decay leptonically. The kinematic depends on the value of the mediator mass, so different selections are developed to target low and high mediator mass scenarios, called DM-SRL and DM-SRH respectively. The differences between the pseudoscalar and scalar mediator kinematics are comparatively minor and do not require a separate optimisation (there is, however, a significant difference in the production cross section).

The selection criteria for the dark matter signal regions are shown in Table 3. Events with same-flavour leptons compatible with the decay of a Z boson are vetoed if $71 < m_{\ell\ell} < 111 \text{ GeV}$. At least one jet is required to be identified as a b -jet, and the angle between the missing transverse momentum and $\mathbf{p}_{\text{miss}}^{\ell\ell}$ has to be smaller than 1.0 radians. This requirement is especially helpful in reducing the $Z/\gamma^* + \text{jets}$ background. The $m_{\text{T}_2}^{ll}$ is required to be larger than 120 GeV, and $E_{\text{T}}^{\text{miss}}$ must be larger than 180 GeV and 260 GeV for SRL and SRH, respectively.

³ The range of the $m_{\ell\ell}$ window has been separately optimised in the three-body search.

Table 3: Summary of dark matter signal region definitions. The trigger, trigger-related lower cuts on lepton p_T , and invariant mass cuts described in the text are applied for all regions. The criteria on $|m_{\ell\ell} - m_Z|$ are applied only to same-flavour events.

Variable	DM-SRL	DM-SRH
$ m_{\ell\ell} - m_Z $ [GeV] (SF only)	>20	>20
b -jet multiplicity	> 0	> 0
$\Delta\phi_{\text{boost}}$	< 1.0	< 1.0
m_{T2}^{ll} [GeV]	>120	>120
$E_{\text{T}}^{\text{miss}}$ [GeV]	> 180	> 260

5 Samples of simulated events

Sample of simulated events are used to model the SUSY signal and those SM backgrounds with two or more real leptons in the final state. The samples include an ATLAS detector simulation [62], based on GEANT4 [63], or a fast simulation that uses a parameterisation of the calorimeter response and GEANT4 for the other parts of the detector [64]. The simulated events are reconstructed with the same algorithms as used for the data.

Diboson processes with two to four charged leptons are produced using the **SHERPA** v2.1.1 [65] generator [66]. The matrix elements contain the doubly-resonant WW , WZ and ZZ processes and all other diagrams with four or six electroweak vertices (such as $WWjj$). The $3\ell + 1\nu$ process is calculated at NLO in QCD, additional diagrams involving up to three extra partons at LO are calculated using the **Comix** [67] and **OPENLOOPS** [68] matrix element generators and merged with the **SHERPA** parton shower [69] using the **ME+PS@NLO** prescription [70]. Fully leptonic triboson processes (WWW , WWZ , WZZ and ZZZ) with up to six charged leptons are also produced using **SHERPA** v2.1.1. The $WWZ \rightarrow 4\ell + 2\nu$ or $2\ell + 4\nu$, $WZZ \rightarrow 3\ell + 3\nu$ or $5\ell + 1\nu$, $ZZZ \rightarrow 6\ell + 0\nu$, $4\ell + 2\nu$ or $2\ell + 4\nu$ processes are calculated with the same configuration as the diboson samples, but with up to only two extra partons at LO. The **CT10** [71] parton distribution function (PDF) set is used for all **SHERPA** samples in conjunction with a dedicated parton shower tuning developed by the **SHERPA** authors. The theoretical cross sections are used when normalising the diboson and tri-boson backgrounds.

For the production of $t\bar{t}$ and single top-quarks in the Wt channel, the **POWHEG-Box** v2 generator with the **CT10** PDF set is used [72]. The top quark mass is assumed to be 172.5 GeV. The $t\bar{t}$ (single top) events are normalised to the **NNLO + NNLL QCD** [73] (NLO) cross sections.

Events containing Z bosons with associated jets ($Z/\gamma^* + \text{jets}$) are produced using the **SHERPA** v2.2 generator with massive b/c-quarks to improve the treatment of the associated production of Z bosons with heavy flavour jets [74]. Matrix elements are calculated for up to two partons at NLO and up to four partons at leading order (LO). The matrix elements are calculated using the **Comix** and **OPENLOOPS** generators of matrix elements and merged with the **SHERPA** parton shower using the **ME+PS@NLO** prescription. The **CT10** PDF set is used in conjunction with a dedicated parton shower tuning developed by the **SHERPA** authors. A global k -factor is used to normalise the $Z/\gamma^* + \text{jets}$ events to the **NNLO QCD** cross sections.

Samples of $t\bar{t} + V$ (with $V = W$ and Z , including non-resonant Z/γ^* contributions) and $t\bar{t} + WW$ production are generated at LO with **MADGRAPH5_aMC@NLO** [75] v2.2.2 interfaced to the **PYTHIA** 8.186 [76] parton

shower model [77]. Events from $t\bar{t} + W$ and $t\bar{t} + Z$ were generated including respectively up to two and one extra partons in the matrix element. No additional partons were included in the $t\bar{t} + WW$ generation. The A14 tune [78] was used together with the NNPDF23LO PDF set [79]. The $t\bar{t} + W$, $t\bar{t} + Z$, $t\bar{t} + WW$ events are normalised to their NLO cross section [75].

The production of a Higgs boson in association with a $t\bar{t}$ pair is generated using `MADGRAPH5_aMC@NLO` [75] v2.2.2 interfaced to `HERWIG` 2.7.1 [80]. The UEEE5 underlying event tune is used together with the CTEQ6L1 [81] (matrix element) and CT10 (parton shower) PDF sets. Samples of SM Higgs boson events in association with a W or Z boson are produced with `PYTHIA` 8.186, using the A14 tune and the NNPDF23LO PDF set. Events are normalised to cross sections calculated at NLO QCD [82].

The SUSY signal samples are generated using LO matrix elements with up to two extra partons, with the `MADGRAPH5_aMC@NLO` [75] v2.2.3 generator. The modelling of the SUSY decay chain, parton showering, hadronisation and the description of the underlying event are simulated with `PYTHIA` 8.186, using the A14 tune. Parton luminosities are provided by the NNPDF23LO PDF set. The jet-parton matching is realised following the CKKW-L prescription [83], with a matching scale set to one quarter of the pair-produced superpartner mass. Signal cross sections are calculated to next-to-leading order in the strong coupling constant, adding the resummation of soft gluon emission at next-to-leading-logarithmic accuracy (NLO+NLL) [84–86]. The nominal cross section and the uncertainty are taken from an envelope of cross section predictions using different PDF sets and factorisation and renormalisation scales, as described in Ref. [87]. The production cross section of top squark pairs with a mass of 500 GeV is 518 fb at $\sqrt{s} = 13$ TeV (compared with 86 fb at $\sqrt{s} = 8$ TeV).

The DM signal samples are generated from LO matrix elements with no extra partons, using the `MG5_aMC` generator. `PYTHIA` 8.186, with the A14 tune, is used for the modelling of the parton showering, hadronisation and the description of the underlying event. Parton luminosities are provided by the NNPDF30LO PDF set. The ME–PS matching is done using the CKKW-L [88] prescription. Signal cross sections are calculated to LO accuracy [25].

In all samples of simulated events, except those produced by `SHERPA`, the `EvtGEN` v1.2.0 program [89] is used to model the properties of the bottom and charm hadron decays. To simulate the effects of additional pp collisions in the same and nearby bunch crossings, additional interactions are generated using the soft QCD processes of `PYTHIA` 8.186 with the A2 tune [90] and the MSTW2008LO PDF [91], and overlaid onto the simulated hard scatter event. The samples of simulated events are reweighted so that the distribution of the average number of proton-proton interactions per bunch crossing matches the observed distribution in the data. Corrections derived from data control samples are applied to simulated events to account for differences between data and simulation in the reconstruction efficiencies, momentum scale and resolution of leptons and in the efficiency and false positive rate for identifying b -jets.

6 Background Estimation

For each SR, the normalisation of the dominant irreducible SM background processes is obtained by normalising the yield to the observed data in a background dominated control selection (CR), and then extrapolating this yield to the SRs as described below. Smaller irreducible background processes are predicted using solely estimates from simulation.

For each SR, a simultaneous “background” fit is performed to the number of events found in the CRs to determine the SM process normalisations, using the `HistFitter` package [92]. When setting 95% CL upper

limits on the cross section of specific signal models, the simultaneous fits also include the observed yields in the SR. In each fit, the normalisations of the major irreducible background contributions are allowed to float, while the other backgrounds are determined directly from their yields using the corresponding theoretical cross sections.

The signal regions for the three-body, hadronic m_{T2} and dark matter selections are populated by different background processes and thus use different CRs. The definition of the regions used in each analysis and the results of the fit are described in the next subsections.

The background due to fake and non-prompt leptons, collectively referred to as “FNP”, is small (less than 10% of the total background). It consists of semi-leptonic $t\bar{t}$, s -channel and t -channel single top, W +jets and light- and heavy-flavour multijet events. It is commonly estimated from data with a method similar to that described in Refs. [93, 94]. Two types of lepton identification criteria are defined for this evaluation: “tight”, corresponding to signal leptons described above, and “loose”, corresponding to candidate electrons and muons. The method makes use of the number of observed events containing loose-loose, loose-tight, tight-loose and tight-tight lepton pairs in a given SR. The probability for prompt leptons passing the loose selection criteria to also pass the tight selection is measured using a $Z \rightarrow \ell\ell$ ($\ell = e, \mu$) sample. The equivalent probability for fake or non-prompt leptons is measured from multi-jet-enriched control samples. The number of events containing a contribution from one or two fake and non-prompt leptons is calculated from these probabilities.

Systematic uncertainties in the samples of simulated events affect the ratio of the expected yields in the different regions and are taken into account to determine the uncertainty on the background prediction. The systematic uncertainties are described by nuisance parameters, which are not constrained by the fit, since the number of floating background normalisation is equal to the number of CRs. Each uncertainty source is described by a single nuisance parameter, and all correlations between background processes and selections are taken into account. The list of systematic uncertainties considered in the fit is described in Section 7.

6.1 Hadronic m_{T2} background estimate

The largest backgrounds in the hadronic m_{T2} signal region are expected to be top pair production and single top (Wt) production. For these backgrounds, two CRs that are statistically independent of the SRs are defined. Each CR is enriched in the targeted background source and used to constrain its normalisation with data. The extrapolation of the top background rates from the CR to the SRs relies on the samples of simulated events, which is also used for the prediction of the smaller backgrounds with two prompt leptons (Z/γ^*+jets , dibosons, $t\bar{t}V$ and Higgs processes).

In order to reduce the potential signal contamination, m_{T2}^{bb} is required to be lower than 160 GeV, bringing the expected signal contribution below a 8% of the total expected yields in the CRs. The top pair production CR (CR $t\bar{t}bar$) also applies a lower cut on m_{T2}^{bb} , in order to probe a kinematic regime closer to the SRs. This is not done in the single top CR (CR st) because of the limited number of expected events after the CR st selection. Relative to the SRs, the CRs also drop requirement on the leading lepton p_T in order to increase the event yield. In order to separate the single top and top pair production, the following variable, based on the invariant mass between each lepton and b -jet, is considered:

$$m_{bl}^{\min} = \min((\max(m_{b_1 l_1}, m_{b_2 l_2}), \max(m_{b_1 l_2}, m_{b_2 l_1})))$$

Table 4: Definition of the control and validation regions in the hadronic m_{T2} selection. A horizontal dash indicates that no selection is applied. The trigger, trigger-related lower cuts on lepton p_T and E_T^{miss} , and invariant mass cuts described in the text are applied for all regions.

Variable	CRttbar	CRst	VRttbar	VRst
m_{T2}^{bb} [GeV]	$>120 \& <160$	<160	$>160 \& <220$	$>160 \& <220$
b -jet multiplicity	$= 2$	$= 2$	$= 1$	$= 2$
$E_{T,\text{min}}^{\text{bl}}$ [GeV]	-	-	-	-
$m_{\text{min}}^{\text{bl}}$ [GeV]	<170	>170	-	-
E_T^{miss} [GeV]	-	-	-	< 200

Two validation regions are defined, in order to validate the extrapolation from the CRs to the SRs, that are enriched in single top (VRst) and top pair (VRttbar) production, respectively. VRttbar requires exactly one b -jet in order to reduce the potential signal contamination, which is expected to be below 6%. At least one more jet is required in the event, and the jet with the highest b -tagging weight among those failing the selected working point is used together with the identified b -jet in the calculation of m_{T2}^{bb} . For $t\bar{t}$ events in CRttbar, most of the selected b -jets are true b -jets from the top quark decay. Such events have a kinematic endpoint in m_{T2}^{bb} and mostly fail to enter the SRs, since the latter is enriched in events with at least one mis-tagged jet. VRttbar is constructed such that selects events with a flavour composition similar to that of the SRs. VRst requires exactly two b -jets, like CRst and the SR. In all these regions, the majority of the selected single top events have two real b quarks. The CR and VR definitions are given in Table 4.

Figure 2 shows the m_{T2}^{bb} and $m_{\text{min}}^{\text{bl}}$ distributions after applying the CRs selection but without including the requirements on the m_{T2}^{bb} or $m_{\text{min}}^{\text{bl}}$. Good agreement is observed between data and simulation at the preselection level and in the different CRs. The m_{T2}^{bb} distribution in data presents a deficit for values above 160 GeV, which corresponds to the upper cut on the CRst definition, still compatible, within about one standard deviation, with the background predictions. Similar effect is observed in the validation region.

The background rate in all regions is determined by a background fit, as previously described. Table 5 presents, for the control and validation regions, the expected yields before and after the background fit is performed. The result for the SRs is reported in Section 8.1.

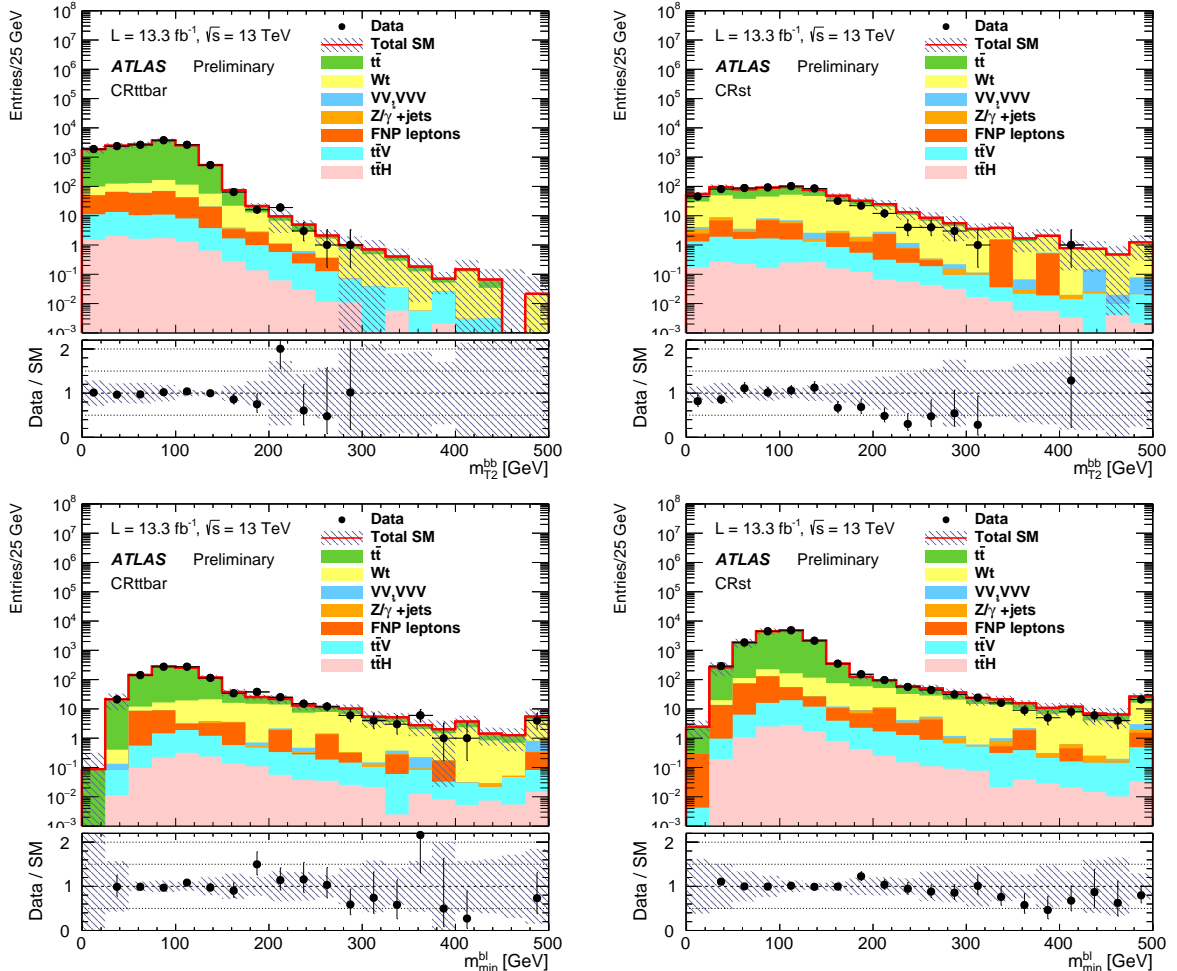


Figure 2: Distribution of m_{T2}^{bb} for events passing the CRttbar (top left) and the CRst selection (top right), except for the m_{T2}^{bb} cut itself, and distribution of m_{min}^{bl} for events passing the CRttbar (bottom left) and the CRst selection (bottom right), except for the m_{min}^{bl} cut itself. The figures use 13.3 fb^{-1} of pp collision data. The normalisation of the top backgrounds comes from the likelihood fit described in the text, and the uncertainty band includes statistics and systematics uncertainties.

Table 5: Background fit results for the CRs and VRs in the hadronic m_{t2} search for an integrated luminosity of 13.3 fb^{-1} . For backgrounds whose normalisation is determined by the fit and for the total background the nominal expectations from simulation (MC) are given in the lower portion of the table. Combined statistical and systematic uncertainties are shown. Uncertainties on the predicted background event yields are quoted as symmetric except where the negative error reaches down to zero predicted events, in which case the negative error is truncated.

	CRttbar	CRst	VRttbar	VRst
Observed	849	512	545	48
Total Standard Model	849 ± 29	512 ± 22	530 ± 152	65.3 ± 18
Fitted $t\bar{t}$	767 ± 43	236 ± 94	390 ± 180	23 ± 17
Fitted Wt	54 ± 28	240 ± 97	100 ± 51	38 ± 21
Diboson	0.43 ± 0.13	3.76 ± 0.67	9.9 ± 1.3	0.20 ± 0.16
$Z/\gamma^*+\text{jets}$	0.73 ± 0.72	5.0 ± 3.0	5.0 ± 3.6	0.75 ± 0.59
Fakes and non-prompt	21.1 ± 5.6	17.7 ± 5.1	20.2 ± 5.1	2.0 ± 1.6
$t\bar{t}$ V	4.71 ± 0.31	8.3 ± 1.1	4.72 ± 0.49	0.98 ± 0.11
$t\bar{t}$ H	1.00 ± 0.15	1.41 ± 0.18	0.44 ± 0.10	0.30 ± 0.04
MC exp. Standard Model	848	460	520	57
MC exp. $t\bar{t}$	777	239	400	23
MC exp. Wt	42	185	77	30

6.2 Three-body background estimate

In the three-body signal regions defined in Section 4.3, the SM background is dominated by diboson and $t\bar{t}$ production. The SM predictions are taken from simulation for the most significant backgrounds are normalised to data in dedicated control regions. The major contribution to diboson production in the SF regions is coming from ZV production, whereas in the DF regions it is coming from WW production. Therefore, one dedicated control region is constructed for each dilepton flavour combination. Conversely, the $t\bar{t}$ production is flavour symmetric, for which only a single control region is used. The FNP background is estimated using the matrix method described earlier. Finally, contributions from remaining sources of SM background, which include Higgs boson production and Z/γ^*+jets , are small and are estimated from samples of simulated events. The background predictions are tested in validation regions that are defined to be kinematically adjacent to, yet disjoint from, the signal regions. The definitions of the control and validation regions are shown in Table 6. In all control and validation regions the signal contamination is less than 17%.

Table 6: Definitions of the control and validation regions for the three-body search. SF refers to same-flavour (ee and $\mu\mu$), and DF to different-flavour ($e\mu$) lepton pairs.. The common selection defined in Section 4.3 also applies to all regions.

Selection	CR-Top	CR-VV-DF	CR-VV-SF	VR-Top	VR-VV-DF	VR-VV-SF
Lepton flavour	DF	DF	SF	DF	DF	SF
b -jet multiplicity	>0	$== 0$	$== 0$	$== 0$	$== 0$	$== 0$
M_Δ^R [GeV]	> 80	> 30	> 30	> 80	$(30, 80)$	$(30, 80)$
R_{p_T}	> 0.5	< 0.5	< 0.5	< 0.5	< 0.5	< 0.5
$1/\gamma_{R+1}$	–	> 0.8	> 0.8	–	> 0.8	> 0.8
E_T^{miss} [GeV]	–	–	> 70	–	–	> 70
$(\cos \theta_b, \Delta\phi_\beta^R)$	$\Delta\phi_\beta^R < (0.85 \times \cos \theta_b + 1.8)$			$\Delta\phi_\beta^R > (0.85 \times \cos \theta_b + 1.8)$		

Table 7 shows the expected and observed number of events in each of the control and validation regions after the background fit. As can be seen, the number of total fitted background events in the validation regions is in agreement with the observed number of data events. Figure 3 shows a selected number of distributions in the control regions for this analysis.

Table 7: Background fit results for the CRs and VRs in the three-body search for an integrated luminosity of 13.3 fb^{-1} . For backgrounds whose normalisation is determined by the fit and for the total background the nominal expectations from simulation (MC) are given in the lower portion of the table. Combined statistical and systematic uncertainties are shown. Uncertainties on the predicted background event yields are quoted as symmetric except where the negative error reaches down to zero predicted events, in which case the negative error is truncated.

Region	CR-Top	CR-VV-DF	CR-VV-SF	VR-Top	VR-VV-DF	VR-VV-SF
Observed events	2434	533	314	212	186	196
Total Standard Model	2430 ± 50	533 ± 23	314 ± 18	254 ± 22	198 ± 13	200 ± 120
Fitted $t\bar{t}$	2190 ± 50	113 ± 12	70 ± 11	122 ± 8	32 ± 4	29 ± 6
Wt	220 ± 18	40 ± 5	22 ± 4	22.7 ± 2.6	10.3 ± 1.1	8.2 ± 1.7
$t\bar{t}+V$	8.0 ± 0.9	0.11 ± 0.02	0.12 ± 0.02	0.32 ± 0.06	0.0 ± 0.0	0.01 ± 0.01
Fitted VVDF	19 ± 4	343 ± 27	—	102 ± 19	134 ± 14	—
Fitted VVSF	—	—	129 ± 31	—	—	86 ± 31
$Z/\gamma^*+\text{jets}$	0.51 ± 0.30	1.1 ± 0.8	90 ± 17	0.02 ± 0.01	—	60^{+110}_{-60}
Fake and non-prompt	—	34.8 ± 1.3	4.8 ± 0.5	7.10 ± 0.27	21.0 ± 0.9	11.8 ± 2.2
MC exp. Standard Model	2443	461	291	233	169	180
MC exp. $t\bar{t}$	2198	114	70	123	32	29
MC exp. VVDF	15.3	271	—	80	106	—
MC exp. VVSF	—	—	105	—	—	70

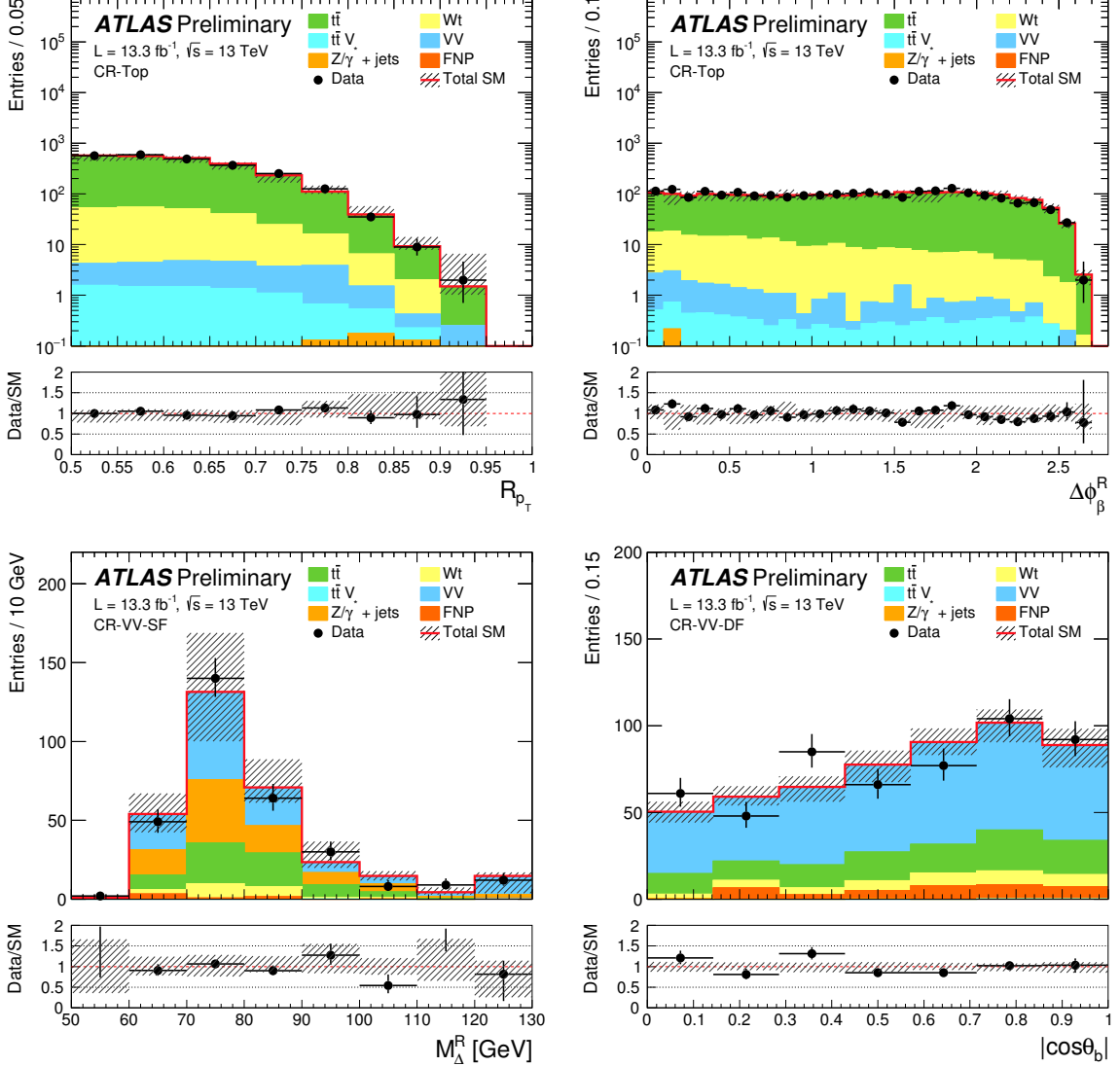


Figure 3: Distributions of R_{p_T} (top-left) and $\Delta\phi_\beta^R$ (top-right) in CR-Top, M_Δ^R (bottom-left) in CR-VV-SF, and $\cos\theta_b$ (bottom-right) in CR-VV-DF. The hashed regions represent the total uncertainties on the background estimates. The rightmost bin of each plot includes overflow events. The lower panel of each plot shows the ratio of the data to the SM background prediction. The normalisations of the $t\bar{t}$ and VV processes come from the likelihood fit described in the text.

6.3 Dark matter background estimate

In this case, the largest SM background contribution is originated by top production events, particularly from $t\bar{t}$ and $t\bar{t}+Z$ events. These two sources are estimated simultaneously. Control regions, rich in these processes and with negligible signal contamination, are created in the m_{T2}^{ll} vs lepton multiplicity plane. $t\bar{t}+Z$ events can have more than 2 leptons (which defines the CRTZ control region), whilst the low m_{T2}^{ll} region is rich in $t\bar{t}$ events whilst being poor in expected signal events (leading to the CRT control region). In CRTZ, where three or more leptons are present, m_{T2}^{ll} is chosen to be the largest value obtained from all possible two lepton combinations. By extrapolating from the CRs to the SR the background estimation is obtained. The definition of the CRs is given in Table 8.

Table 8: Summary of control and validation region definitions for the dark matter search.

Selection	CRT	CRTZ	VRVV	VRMET	VRMT2	VRINC
m_{T2}^{ll} [GeV]	60-100	>90	>100	–	>120	–
b -jet multiplicity	> 0	> 0	0	> 0	> 0	> 0
Jet multiplicity	> 1	> 1	> 1	> 1	> 1	–
Lepton multiplicity	2	> 2	2	2	2	2
$\Delta\phi_{\text{boost}}$	< 1	–	–	> 1	> 1	> 1
E_T^{miss} [GeV]	–	–	–	> 180	–	–

Table 9: Background fit results for the CRs and VRs in the dark matter search for an integrated luminosity of 13.3 fb^{-1} . For backgrounds whose normalisation is determined by the fit and for the total background the nominal expectations from simulation (MC) are given in the lower portion of the table. Combined statistical and systematic uncertainties are shown. Uncertainties on the predicted background event yields are quoted as symmetric except where the negative error reaches down to zero predicted events, in which case the negative error is truncated.

	CRT	CRTZ	VRVV	VRMET	VRMT2	VRINC
Observed events	6758	26	100	30	71	10802
Total Standard Model	6758 ± 83	26.0 ± 5.1	90 ± 20	30.3 ± 3.8	53.3 ± 9.0	10600 ± 1000
Fitted $t\bar{t}$	6460 ± 89	–	39 ± 17	21.0 ± 4.6	20 ± 6.3	9700 ± 1000
Wt	264 ± 24	–	5.8 ± 1.8	4.9 ± 2.0	3.6 ± 1.5	847 ± 12
$Z/\gamma^*+{\text{jets}}$	$0.05^{+0.06}_{-0.05}$	–	$0.06^{+0.08}_{-0.06}$	1.26 ± 0.29	18.8 ± 3.4	47.7 ± 9.5
VV	12.4 ± 2.3	3.65 ± 0.92	40.9 ± 3.4	0.77 ± 0.31	6.2 ± 1.4	40.2 ± 5.6
Fitted $t\bar{t} Z$	6.9 ± 2.9	14.5 ± 5.8	0.46 ± 0.21	0.63 ± 0.27	1.85 ± 0.79	11.0 ± 4.6
$t\bar{t} W$	8.02 ± 0.28	2.44 ± 0.17	0.28 ± 0.06	0.34 ± 0.05	0.92 ± 0.10	10.88 ± 0.59
Fake and non prompt leptons	$1.7^{+1.7}_{-1.7}$	3.5 ± 2.5	$2.5^{+2.8}_{-2.5}$	1.3 ± 1.3	$1.1^{+1.5}_{-1.1}$	–
Other processes	5.59 ± 0.18	2.05 ± 0.17	0.14 ± 0.03	0.14 ± 0.02	0.93 ± 0.44	8.09 ± 0.61
MC exp. Standard Model	6500	30	88	28	34	10100
MC exp. $t\bar{t}$	6150	–	37	20	19	9200
MC exp. $t\bar{t} Z$	8.76	18.4	0.58	0.80	2.0	14

Figure 4 shows the comparison of the data with the background prediction for the m_{T2}^{ll} variable in CRTZ and the jets multiplicity in CRT. The data is in good agreement with a background-only prediction within uncertainties.

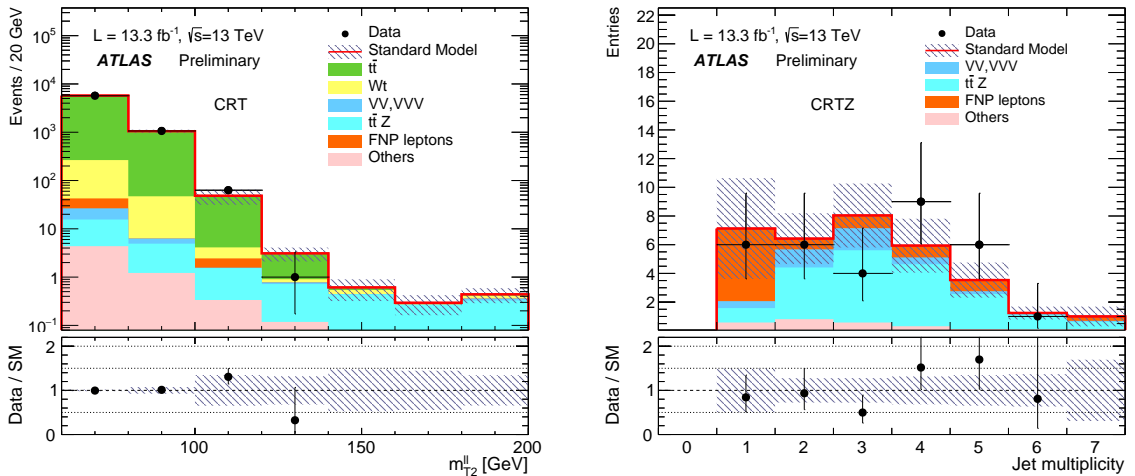


Figure 4: m_{T2} distribution in CRT (left) and jet multiplicity distribution in CRTZ (right) for an integrated luminosity of 13.3 fb^{-1} . The CR selections on the plotted variables are not applied in the figure. The contributions from all SM backgrounds are shown as a histogram stack; the bands represent the total uncertainty from statistical and systematic sources. The normalisations of the $t\bar{t}$ and $t\bar{t}Z$ processes come from the likelihood fit described in the text.

Four different validation regions are defined by inverting some of the selection requirements. The regions VRVV, VRMET, VRMT2, and VRINC are used to validate, respectively, the diboson contribution, the $E_{\text{T}}^{\text{miss}}$ modelling at high m_{T2}^{ll} , the m_{T2}^{ll} modelling at high $E_{\text{T}}^{\text{miss}}$ and an inclusive selection orthogonal to the SRs. The detailed definition of each of the validation regions is provided in Table 8.

Table 9 shows the results in the control and validation regions after the background fit. A good agreement is found between data and predictions in the validation regions. In the case of VRMT2, the data is above the predictions by less than two standard deviations and the effect is still attributed to a statistical fluctuation.

7 Systematic Uncertainties

The primary sources of systematic uncertainty are related to: the jet energy scale (JES) and resolution (JER), the b -tagging calibration, the modelling in the simulated event samples, the re-weighting procedure applied to simulation for matching the distribution of the average number of proton-proton interactions per bunch crossing observed in data, and the cross section uncertainties. The uncertainty related to the finite yields of the simulated event samples is taken into account as well. The effects of these uncertainties are evaluated for all signal samples and background processes. Since the normalisation of the dominant background contributions is extracted in dedicated control regions, in these cases the uncertainties only affect the extrapolation from the control to the signal regions.

The JES and JER uncertainties are derived as a function of the p_{T} and η of the jet, as well as of the pileup conditions and the jet flavour composition of the selected jet sample. They are determined using a combination of simulated and data samples, through measurements of the jet response asymmetry in dijet, Z+jet and γ +jet events [95]. The systematic uncertainties related to the modelling of $E_{\text{T}}^{\text{miss}}$ in the simulation are estimated by propagating the uncertainties on the energy and momentum scale of each of

the physics objects, as well as the uncertainties on unclustered soft contributions [55]. The efficiencies for the b -tagging of true b , charm, and light jets are measured in data [96, 97] and their uncertainty accounted separately in the fit. The remaining detector-related systematic uncertainties, such as those on lepton reconstruction efficiency, energy scale, energy resolution and on the modelling of the trigger [46, 47] are negligible.

The uncertainties coming from the background modelling in the simulated event samples are estimated for dibosons processes by varying the renormalisation, factorisation, resummation and matrix-elements to parton shower matching scales used to generate the samples. For $t\bar{t}$ and Wt , the uncertainties related to the modelling of the hard scattering process are evaluated by comparing the nominal Powheg predictions with the ones from `MADGRAPH5_aMC@NLO`, using the `PYTHIA` showering in both cases. The uncertainties related to the modelling of initial- and final-state radiation are derived by comparing samples with a different amounts of radiation with the nominal sample. The modified samples are generated varying the factorisation and renormalisation scales and the cutoff scale for the first gluon emission (h_{damp} parameter) by a factor of two.

Finally, the uncertainty associated to the parton shower modelling is assessed as the difference between the predictions from Powheg + Pythia and Powheg + Herwig++. An additional systematics on the interference between $t\bar{t}$ and single top is assigned with the extreme choice of neglecting the interference completely with the diagram removal scheme and comparing the results with those of the nominal $t\bar{t}$ sample. The resulting uncertainty is significant, but not dominant, for the hadronic m_{T2} selection and negligible for the other selections (see Table 10).

The uncertainties related to the choice of the QCD renormalisation and factorisation scales in $Z/\gamma^*+{\text{jets}}$ events are assessed by varying the corresponding generator parameters up and down by a factor of two around their nominal values. Uncertainties on the resummation scale and the matching scale between the matrix element and the parton shower are evaluated by varying up and down by a factor of two the corresponding parameters in `SHERPA`.

The theoretical uncertainties on the predicted cross section, used to normalise background processes from simulations, are taken into account. This includes a 5.3% uncertainty for single top Wt -channel [98], a 6% for diboson, a 13% for $t\bar{t}+W$ and a 12% for $t\bar{t}+Z$ production [75]. For the $t\bar{t}+WW/Z$, $t\bar{t}+h$ and triboson production processes, which constitute a small background in all signal regions, a 50% uncertainty on the event yields is assumed.

Two sources of systematic uncertainty are assigned to the fake and non-prompt lepton background estimate. The first one takes into account the potentially different FNP compositions (heavy flavour, light flavour or conversions) between the signal and control regions. The second one account for variations of the contamination from prompt leptons in the regions used to measure the probabilities for loose fake and non-prompt leptons to pass the tight signal criteria.

A summary of the leading systematic uncertainties on the total expected background is given in Table 10, as determined after the background fit.

Table 10: Sources of systematic uncertainty on the SM background estimates, evaluated after the background fit. The values are given as relative uncertainties on the expected background event yields in the SRs. Entries marked “–” indicate either a negligible contribution or an uncertainty that does not apply (for example the normalisation uncertainty for a background whose normalisation is not fitted for that specific signal region). MC statistics refer to the statistical uncertainty from the simulated event samples. The individual components can be correlated and therefore do not necessarily add up in quadrature to the total systematic uncertainty. The total number of expected background events is also shown.

Signal Region	SR _{Low} ^{hadMT2}	SR _{High} ^{hadMT2}	SR _W ^{3-body} -SF	SR _W ^{3-body} -DF	SR _t ^{3-body} -SF	SR _t ^{3-body} -DF	DM-SRL	DM-SRH
Total background expectation	13.6	6.8	12	5.3	4.7	3.7	6.4	2.27
Total background systematic	50%	58%	34%	41%	41%	41%	36%	26%
Jet energy scale	–	–	16%	23%	17%	9%	6%	4%
Jet energy resolution	–	–	2%	10%	2%	11%	3%	5%
E_T^{miss} modelling	1%	1%	–	–	–	–	2%	1%
MC statistical uncertainties	3%	5%	13%	20%	13%	25%	5%	–
Diboson theoretical uncertainties	–	–	10%	12%	2%	<1%	–	1%
top theoretical uncertainties	30%	29%	17%	22%	34%	30%	10%	23%
$t\bar{t}$ - Wt interference	22%	27%	–	–	–	–	–	–
Diboson fitted normalisation	–	–	15%	3%	2%	<1%	–	–
$t\bar{t}$ fitted normalisation	1%	1%	1%	1%	2%	2%	1%	–
Wt fitted normalisation	26%	26%	–	–	–	–	–	–
$t\bar{t}$ V fitted normalisation	–	–	–	–	–	–	14%	18%
Fake and non-prompt lepton	4%	6%	3%	6%	<1%	15%	–	–
Luminosity	1%	1%	1%	1%	1%	1%	1%	1%

8 Results

The data is compared to background predictions in the signal regions of the different analyses. As discussed below, good agreement is observed between data and background predictions in all cases. Two different sets of exclusion limits are then derived on models for new physics beyond the SM. A model independent upper limit on the visible cross section, defined as cross section times acceptance times efficiency, for new physics is derived in each SR by performing a fit which includes the observed yield in the SR as a constraint, and a free signal yield in the SR as an additional process. The possible signal contamination in the CRs, and the uncertainties on the signal are neglected, since these depend on the model. Model dependent limits are derived on the specific signal scenarios targeted by each analysis. The profile likelihood fit is performed including the expected signal yield and its associated uncertainties in the CRs and SRs, and deriving the exclusion confidence level with the CLs method [99]. Correlation between the shared experimental uncertainties between background and signal uncertainties are accounted for in the fit. All limits are quoted at 95% confidence level.

8.1 Hadronic m_{T2} search

The distribution of m_{T2}^{bb} after all the selections of SR_{Low}^{hadMT2} and the distribution of $E_{T,\text{min}}^{\text{bl}}$ after all the selections of SR_{High}^{hadMT2}, except the selection on the variable which is shown, are reported in Fig. 5. The background fit in the SRs is reported in Table 11. Data has been found to be compatible, within about one standard deviation, with the background predictions.

Model independent 95% CL upper limits on the visible cross section ($\langle\epsilon\sigma\rangle_{\text{obs}}^{95}$) and on the number of signal events (S_{obs}^{95}) are reported in Table 12. Beyond SM signals with a visible cross section larger than about 1 fb are excluded at 95% CL by this selection. Exclusion limits are also placed on the model targeted by the analysis, with the top squark decaying to the lightest chargino, and the chargino subsequently decaying to the lightest neutralino and a (real or virtual) W boson. The limits are provided for two signal grids which vary the neutralino and the lightest top squark masses, and make different assumptions on the mass of the lightest chargino. The first grid assumes that $m(\tilde{\chi}_1^\pm) = 2m(\tilde{\chi}_1^0)$ which is a relation satisfied by models with a bino-like $\tilde{\chi}_1^0$, a wino-like $\tilde{\chi}_1^\pm$, and unification of the gaugino masses at the SUSY breaking scale. The second grid assumes $m(\tilde{\chi}_1^\pm) = 106$ GeV which is just above the limit set by the LEP searches. The results are reported in Figure 6, where for each signal mass point the SR with the best expected limit is used. This is $\text{SR}_{\text{High}}^{\text{hadMT2}}$ at low neutralino and high stop masses, and $\text{SR}_{\text{Low}}^{\text{hadMT2}}$ at high neutralino and low stop masses. Depending on the neutralino and chargino mass, stop masses up to 495 GeV are excluded at 95% CL.

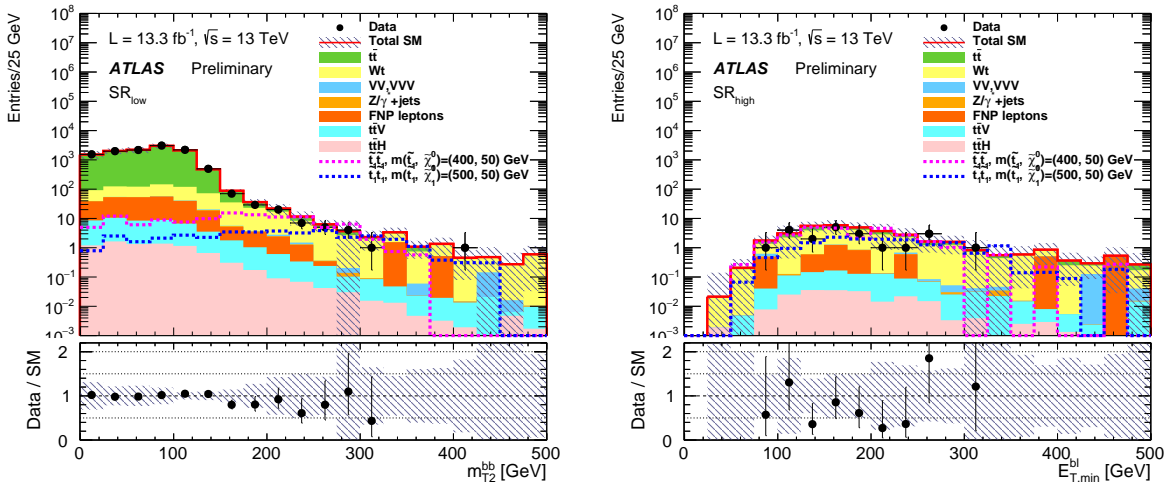


Figure 5: Distributions of m_{T2}^{bb} (left) and $E_{\text{T},\text{min}}^{\text{bl}}$ (right) for events passing the $\text{SR}_{\text{Low}}^{\text{hadMT2}}$ and $\text{SR}_{\text{High}}^{\text{hadMT2}}$ selection respectively, but for the cut on m_{T2}^{bb} or $E_{\text{T},\text{min}}^{\text{bl}}$ itself, and for an integrated luminosity of 13.3 fb^{-1} . The normalisation of the top backgrounds comes from the likelihood fit described in the text, and the uncertainty band includes statistics and systematics uncertainties. Two reference top squark pair production signal models are overlayed for comparison.

Table 11: Results of the background only fit for signal regions for the hadronic m_{T2} signal regions, for an integrated luminosity of 13.3 fb^{-1} . The number of events in each region is reported after the fit and before the fit. The expected number of events for two signal samples ($m(\tilde{t}) = 400 \text{ GeV}$ or 500 GeV , $m(\tilde{\chi}_1^\pm) = 106 \text{ GeV}$, $m(\tilde{\chi}_1^0) = 50 \text{ GeV}$) is also reported.

	$\text{SR}_{\text{Low}}^{\text{hadMT2}}$	$\text{SR}_{\text{High}}^{\text{hadMT2}}$
Observed	21	8
Total Standard Model	35 ± 14	17.3 ± 7.5
Fitted $t\bar{t}$	7.6 ± 3.4	3.3 ± 2.3
Fitted Wt	22 ± 15	11.7 ± 8.3
Diboson	0.44 ± 0.17	0.29 ± 0.15
$Z/\gamma^* + \text{jet}$	0.15 ± 0.12	0.07 ± 0.05
Fakes and non-prompt	3.7 ± 1.5	1.5 ± 1.0
$t\bar{t} V$	0.81 ± 0.10	0.42 ± 0.05
$t\bar{t} H$	0.21 ± 0.03	0.09 ± 0.02
MC exp. Standard Model	30	14.7
MC exp. $t\bar{t}$	7.6	3.4
MC exp. Wt	17	9.0
$\tilde{t}_1 \tilde{t}_1 m(\tilde{t}_1, \tilde{\chi}_1^\pm, \tilde{\chi}_1^0) = (400, 106, 50) \text{ GeV}$	27.4 ± 3.4	12.4 ± 2.5
$\tilde{t}_1 \tilde{t}_1 m(\tilde{t}_1, \tilde{\chi}_1^\pm, \tilde{\chi}_1^0) = (500, 106, 50) \text{ GeV}$	16.2 ± 1.6	10.8 ± 1.1

Table 12: Left to right: 95% CL upper limits on the visible cross section ($\langle \epsilon \sigma \rangle_{\text{obs}}^{95}$) and on the number of signal events (S_{obs}^{95}). The third column (S_{exp}^{95}) shows the 95% CL upper limit on the number of signal events, given the expected number (and $\pm 1\sigma$ excursions on the expectation) of background events. The last column contains the CL_B value, i.e. the confidence level observed for the background-only hypothesis.

Signal channel	$\langle \epsilon \sigma \rangle_{\text{obs}}^{95} [\text{fb}]$	S_{obs}^{95}	S_{exp}^{95}	CL_B
$\text{SR}_{\text{Low}}^{\text{hadMT2}}$	1.18	15.7	$19.2^{+5.8}_{-4.2}$	0.23
$\text{SR}_{\text{High}}^{\text{hadMT2}}$	0.60	8.0	$10.5^{+4.1}_{-2.8}$	0.18

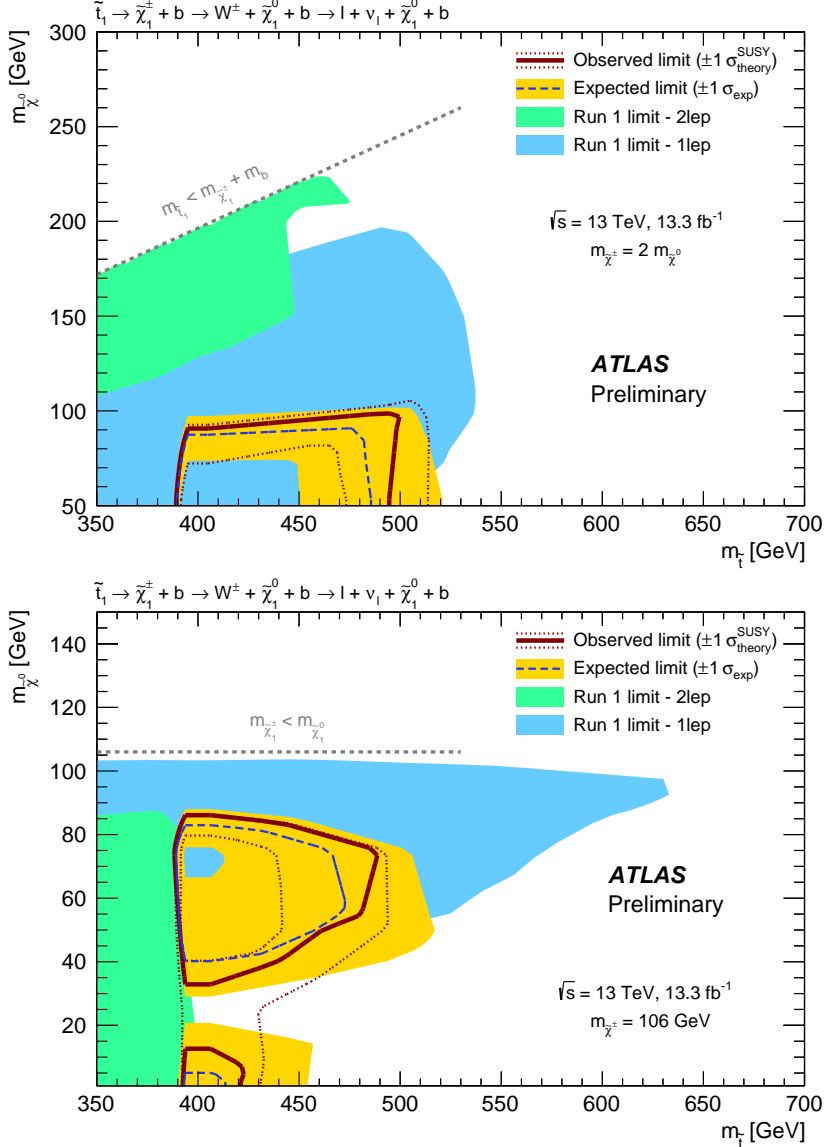


Figure 6: Exclusion plot, for an integrated luminosity of 13.3 fb^{-1} . Grid with $m(\tilde{\chi}_1^\pm) = 2m(\tilde{\chi}_1^0)$ (above) and $m(\tilde{\chi}_1^\pm) = 106 \text{ GeV}$ (below). The dashed line and the shaded band are the expected limit and its $\pm 1\sigma$ uncertainty, respectively. The thick solid line is the observed limit for the central value of the signal cross section. The expected and observed limits do not include the effect of the theoretical uncertainties on the signal cross section. The dotted lines show the effect on the observed limit when varying the signal cross section by $\pm 1\sigma$ of the theoretical uncertainty. The shaded green and blue areas show respectively the observed exclusion from the ATLAS $\sqrt{s} = 8$ TeV analyses performed in the one-lepton (1L) [100] and two-lepton (2L) channels [101].

8.2 Three-body results

In Figure 7 the distribution of M_{Δ}^R is presented in each of the signal regions, split between the same and different flavour channels, omitting the cut on M_{Δ}^R itself. No excess over the SM prediction is visible, and this is reflected in the background-only fit results which are shown for $SR_W^{3\text{-body}}$ in Table 13 and for $SR_t^{3\text{-body}}$ in Table 14. The model independent upper limits are presented in Table 15. Observed yields are within one standard deviation of the background prediction in all SRs. Limits on models with pair production of top squarks, each of them decaying through the three-body mode into $bW\tilde{\chi}_1^0$ are shown in Fig. 8. For a mass difference of $\Delta m(\tilde{t}_1 - \tilde{\chi}_1^0) = 150$ GeV, $SR_t^{3\text{-body}}$ is the most sensitive SR, and stop mass between 250 and 335 GeV are excluded. For a mass difference of $\Delta m(\tilde{t}_1 - \tilde{\chi}_1^0) = 90$ GeV, $SR_W^{3\text{-body}}$ is used and the limits extend up to 365 GeV.

Table 13: Background fit results for the signal region $SR_W^{3\text{-body}}$ in the three-body search for an integrated luminosity of 13.3 fb^{-1} . The nominal expectations from MC simulation are given for each background process in the lower portion of the table. Combined statistical and systematic uncertainties are shown. Uncertainties on the predicted background event yields are quoted as symmetric except where the negative error reaches down to zero predicted events, in which case the negative error is truncated. The expected yields for two signal models are also shown.

Region	$SR_W^{3\text{-body}}\text{-SF}$	$SR_W^{3\text{-body}}\text{-DF}$
Observed events	13	6
Total Standard Model	12 ± 4	5.3 ± 2.2
Fitted $t\bar{t}$	3.9 ± 2.2	2.3 ± 1.4
Wt	0.38 ± 0.16	0.21 ± 0.08
$t\bar{t} V$	0.11 ± 0.03	0.10 ± 0.03
Fitted VVDF	—	2.1 ± 1.1
Fitted VVSF	5.8 ± 2.6	—
$Z/\gamma^* + \text{jets}$	0.79 ± 0.35	—
Fake and non-prompt	0.98 ± 0.13	0.58 ± 0.12
MC exp. Standard Model	11	4.9
MC exp. $t\bar{t}$	3.9	2.3
MC exp. VVDF	—	1.6
MC exp. VVSF	4.8	—
$\tilde{t}_1 \tilde{t}_1 m(\tilde{t}_1, \tilde{\chi}_1^0) = (250, 160)$ GeV	21.8 ± 1.8	18.1 ± 2.0
$\tilde{t}_1 \tilde{t}_1 m(\tilde{t}_1, \tilde{\chi}_1^0) = (300, 150)$ GeV	5.3 ± 0.8	5.1 ± 0.6

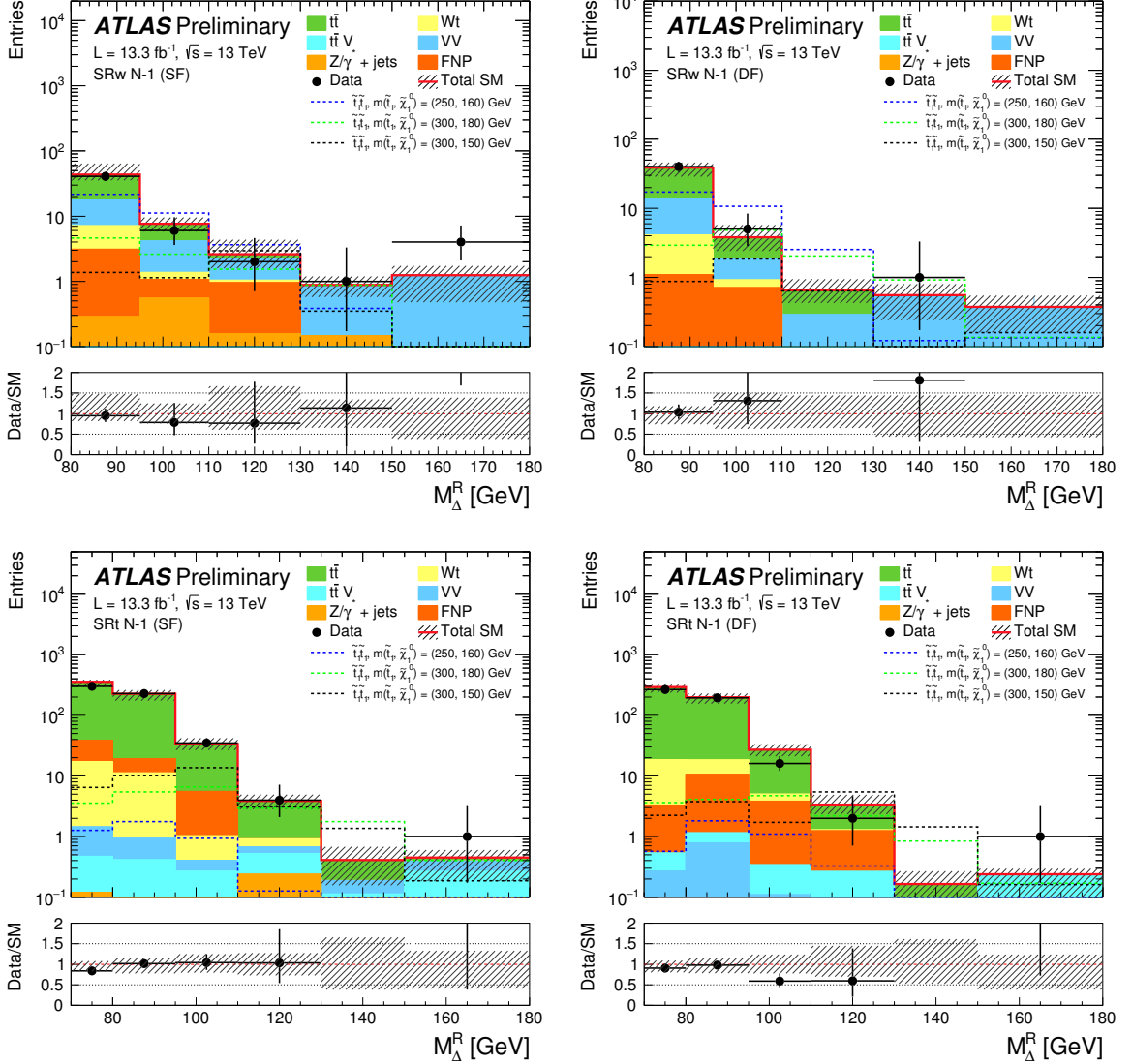


Figure 7: Distributions of the M_{Δ}^R variable in the same flavour (left column) and different flavour (right column) channels of the $SR_W^{3\text{-body}}$ (upper row) and $SR_t^{3\text{-body}}$ (lower row) signal regions, and for an integrated luminosity of 13.3 fb^{-1} . The SR selections on M_{Δ}^R ($SR_W^{3\text{-body}}$ requires $M_{\Delta}^R > 95 \text{ GeV}$ and $SR_t^{3\text{-body}}$ requires $M_{\Delta}^R > 110 \text{ GeV}$) are not applied for these plots. The hashed regions represent the total uncertainties on the background estimates. The rightmost bin of each plot includes overflow events. The lower panel of each plot shows the ratio of the data to the SM background prediction. The normalisations of the $t\bar{t}$ and VV processes come from the likelihood fit described in the text. Three reference top squark pair production signal models are overlayed for comparison.

Table 14: Background fit results for the signal region $SR_t^{3\text{-body}}$ in the three-body search for an integrated luminosity of 13.3 fb^{-1} . The nominal expectations from MC simulation are given for each background process in the lower portion of the table. Combined statistical and systematic uncertainties are shown. Uncertainties on the predicted background event yields are quoted as symmetric except where the negative error reaches down to zero predicted events, in which case the negative error is truncated. The expected yields for two signal models are also shown.

Region	$SR_t^{3\text{-body}}\text{-SF}$	$SR_t^{3\text{-body}}\text{-DF}$
Observed events	5	3
Total Standard Model	4.7 ± 2.0	3.7 ± 1.5
Fitted $t\bar{t}$	3.2 ± 1.8	2.1 ± 1.3
Wt	0.25 ± 0.05	$0.05^{+0.06}_{-0.05}$
$t\bar{t} V$	0.64 ± 0.13	0.55 ± 0.16
Fitted VVDF	—	$0.04^{+0.06}_{-0.04}$
Fitted VVSF	0.35 ± 0.21	—
$Z/\gamma^* + \text{jets}$	0.26 ± 0.14	—
Fake and non-prompt	—	0.90 ± 0.23
MC exp. Standard Model	4.7	3.7
MC exp. $t\bar{t}$	3.3	2.2
MC exp. VVDF	—	0.03
MC exp. VVSF	0.29	—
$\tilde{t}_1 \tilde{t}_1 m(\tilde{t}_1, \tilde{\chi}_1^0) = (250, 160) \text{ GeV}$	0.41 ± 0.16	0.57 ± 0.13
$\tilde{t}_1 \tilde{t}_1 m(\tilde{t}_1, \tilde{\chi}_1^0) = (300, 150) \text{ GeV}$	7.4 ± 1.1	6.7 ± 1.0

Table 15: Left to right: 95% CL upper limits on the visible cross section ($\langle\epsilon\sigma\rangle_{\text{obs}}^{95}$) and on the number of signal events (S_{obs}^{95}). The third column (S_{exp}^{95}) shows the 95% CL upper limit on the number of signal events, given the expected number (and $\pm 1\sigma$ excursions on the expectation) of background events. The last column indicates the CL_B value, i.e. the confidence level observed for the background-only hypothesis.

Region	$\langle\epsilon\sigma\rangle_{\text{obs}}^{95} [\text{fb}]$	S_{obs}^{95}	S_{exp}^{95}	CL_B
$SR_W^{3\text{-body}}\text{-SF}$	0.83	11.1	$10.3^{+4.4}_{-2.9}$	0.57
$SR_W^{3\text{-body}}\text{-DF}$	0.56	7.4	$6.8^{+3.3}_{-2.0}$	0.58
$SR_t^{3\text{-body}}\text{-SF}$	0.47	6.3	$6.1^{+3.2}_{-2.0}$	0.54
$SR_t^{3\text{-body}}\text{-DF}$	0.38	5.1	$5.7^{+2.6}_{-1.8}$	0.39

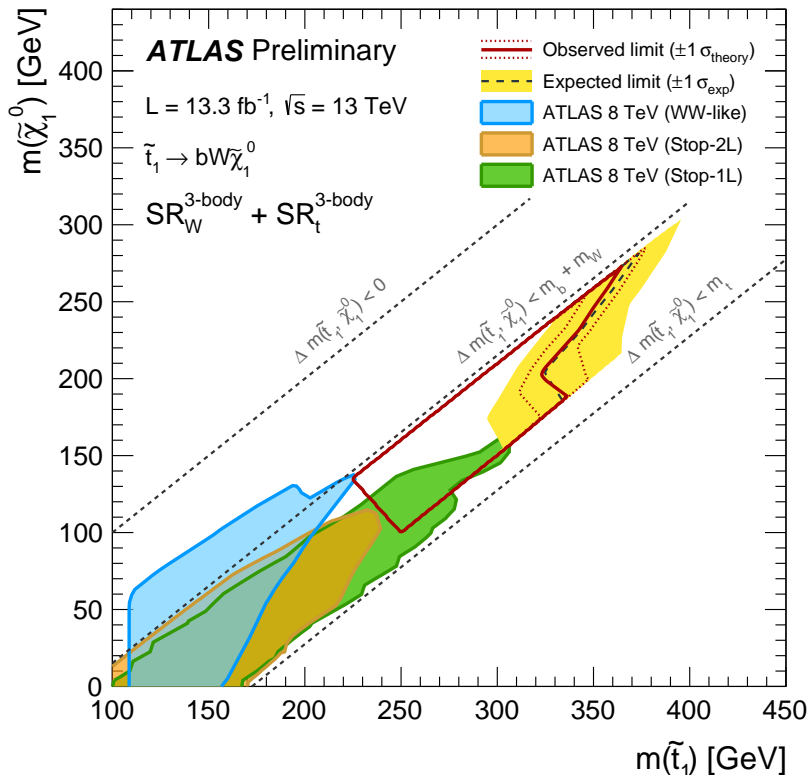


Figure 8: Exclusion contours for \tilde{t}_1 pair production with each \tilde{t}_1 decaying via the three-body process $\tilde{t}_1 \rightarrow bW\tilde{\chi}_1^0$. The $SR_W^{3\text{-body}}$ and $SR_t^{3\text{-body}}$ signal regions are combined in the model dependent fits to provide the result shown here. The dashed line and the shaded band are the expected limit and its $\pm 1\sigma$ uncertainty, respectively. The thick solid line is the observed limit for the central value of the signal cross section. The expected and observed limits do not include the effect of the theoretical uncertainties on the signal cross section. The dotted lines show the effect on the observed limit when varying the signal cross section by $\pm 1\sigma$ of the theoretical uncertainty. The shaded green, orange and azure areas show the observed exclusion from the ATLAS $\sqrt{s} = 8$ TeV searches performed in the one-lepton (Stop-1L) [100], two-lepton (Stop-2L) [101] and WW -like [31] analyses, respectively.

8.3 Dark Matter search

The distribution of E_T^{miss} after all the SR selections except the selection on E_T^{miss} itself, is reported in Fig. 9. The background only fit in the SRs is reported in Table 16. The number of observed events is in good agreement with the background prediction.

As in the other analyses, model independent upper limits are reported in Table 17, these being 0.65 fb and 0.43 fb for SRL and SRH respectively.

Limits on models with dark matter production in association with $t\bar{t}$ are provided for two signal grids which assume respectively either a scalar mediator, shown in Fig. 10, or a pseudoscalar mediator, shown in Fig. 11. Good sensitivity is observed for the on-shell mediator part of the plane ($m(\varphi/a) > 2m(\chi)$). Lower limits on the mediator mass between 300 and 350 GeV are placed for the maximum coupling of $g = 3.5$. For each mass value, the maximum allowed coupling at 95% C.L. is also reported on the plots. For the pseudo scalar case, dark matter particle masses below 60 to 80 GeV are excluded for $g = 3.5$ when $m(a) < 2m(\chi)$.

Table 16: Results of the background only fit for signal regions for the dark matter selection. The number of events in each region is reported after the fit and before the fit. The expected number of events for two signal models, $t\bar{t}\varphi$ (10, 1) and $t\bar{t}\varphi$ (350, 1), is also reported assuming a coupling of $g = 3.5$.

	DM-SRL	DM-SRH
Observed	8	3
Total Standard Model	6.4 ± 2.3	2.27 ± 0.59
Fitted $t\bar{t}$	2.1 ± 1.9	$0.15^{+0.40}_{-0.15}$
Fitted Wt	0.37 ± 0.36	$0.24^{+0.31}_{-0.24}$
$Z/\gamma^* + \text{jets}$	0.15 ± 0.08	0.03 ± 0.03
VV, VVV	0.64 ± 0.22	0.43 ± 0.18
Fitted $t\bar{t} Z$	2.01 ± 0.86	1.00 ± 0.44
$t\bar{t} W$	0.69 ± 0.07	0.27 ± 0.04
Fake and non prompt	$0.00^{+0.35}_{-0.00}$	$0.00^{+0.35}_{-0.00}$
Others	0.42 ± 0.08	0.14 ± 0.04
MC exp. Standard Model	6.7	2.5
MC exp. $t\bar{t}$	2.0	0.14
MC exp. Wt	2.6	1.28
$t\bar{t}\varphi$ (10, 1) GeV, $g = 3.5$	148 ± 57	16^{+19}_{-16}
$t\bar{t}\varphi$ (350, 1) GeV, $g = 3.5$	8.6 ± 1.0	5.23 ± 0.80

Table 17: Left to right: 95% CL upper limits on the visible cross section ($\langle\epsilon\sigma\rangle_{\text{obs}}^{95}$) and on the number of signal events (S_{obs}^{95}). The third column (S_{exp}^{95}) shows the 95% CL upper limit on the number of signal events, given the expected number (and $\pm 1\sigma$ excursions on the expectation) of background events. The last column indicate the CL_B value, i.e. the confidence level observed for the background-only hypothesis.

Signal channel	$\langle\epsilon\sigma\rangle_{\text{obs}}^{95} [\text{fb}]$	S_{obs}^{95}	S_{exp}^{95}	CL_B
DM-SRL	0.65	8.6	$6.8^{+2.3}_{-1.1}$	0.76
DM-SRH	0.43	5.7	$4.5^{+2.1}_{-0.9}$	0.72

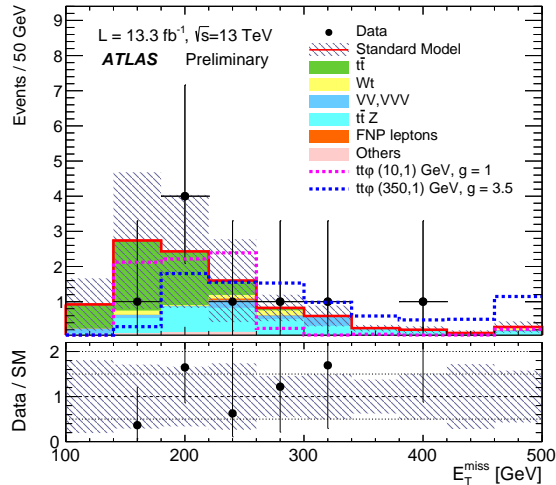


Figure 9: E_T^{miss} distributions for events passing all the signal region requirements but for the selections on E_T^{miss} itself (respectively $E_T^{\text{miss}} > 180$ GeV for DM-SRL and $E_T^{\text{miss}} > 260$ GeV for DM-SRH) for an integrated luminosity of 13.3 fb^{-1} . The contributions from all SM backgrounds are shown as a histogram stack; the bands represent the total uncertainty from statistical and systematic sources. The normalisations of the $t\bar{t}$ and $t\bar{t}Z$ processes come from the likelihood fit described in the text. Two DM signal models assuming scalar mediators are overlaid for comparison.

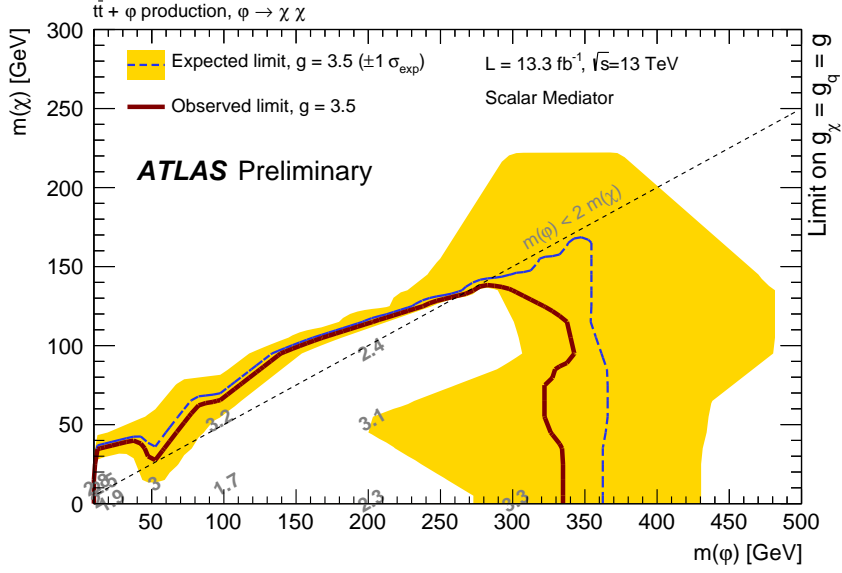


Figure 10: Exclusion limits at 95% CL from the analysis of 13.3 fb^{-1} of 13 TeV collision data on maximum coupling g as a function of the dark matter particle and mediator masses, assuming models with a scalar mediator. The dashed lines are the expected $g = 3.5$ limit and its $\pm 1\sigma$ uncertainty, respectively. The thick solid line is the observed limit for the central value of the signal cross section. The expected and observed limits do not include the effect of the theoretical uncertainties on the signal cross section since they are only known at LO accuracy in QCD.

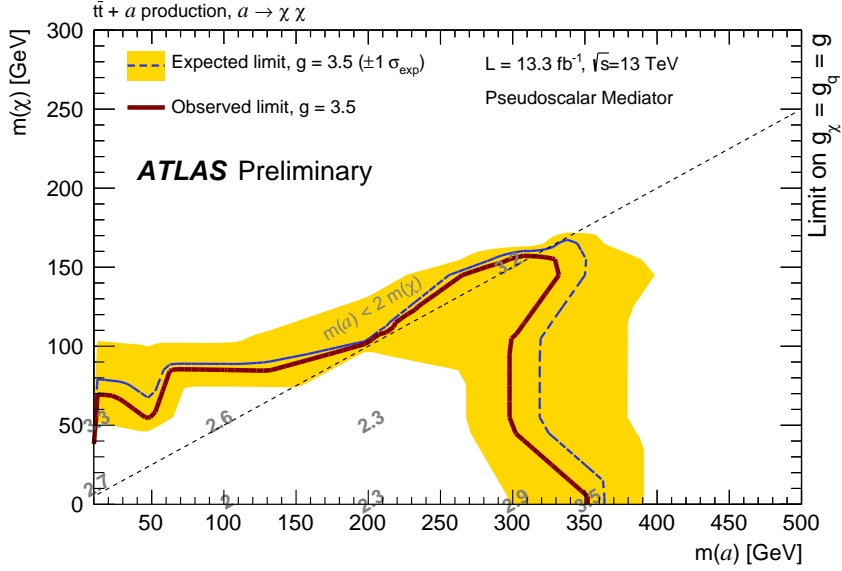


Figure 11: Exclusion limits at 95% CL from the analysis of 13.3 fb^{-1} of 13 TeV collision data on maximum coupling g as a function of the dark matter particle and mediator masses, assuming models with a pseudo-scalar mediator. The dashed lines are the expected $g = 3.5$ limit and its $\pm 1\sigma$ uncertainty, respectively. The thick solid line is the observed limit for the central value of the signal cross section. The expected and observed limits do not include the effect of the theoretical uncertainties on the signal cross section since they are only known at LO accuracy in QCD.

9 Conclusion

This document reports a search for top squark pair production and dark matter production in final states containing two leptons and large missing transverse momentum, based on a 13.3 fb^{-1} dataset of $\sqrt{s} = 13 \text{ TeV}$ proton-proton collisions recorded by the ATLAS experiment at the LHC in 2015 and 2016. Good agreement has been found between the observed events in the data and the expected Standard Model yields.

Model-independent 95% C.L. upper limits on the visible cross section for new phenomena are obtained and vary between 0.38 fb and 1.18 fb , depending on the analysis. The results are also interpreted in terms of simplified models assuming a range of top squark and lightest neutralino masses, with the former decaying to the latter via either a direct three-body decay or via an intermediate chargino state. For a mass difference of 90 GeV between the stop and the neutralino and the three body decay mode, a stop mass below 365 GeV is excluded. The chargino decay mode is excluded for a stop mass between 400 and 495 GeV , a chargino mass of 100 GeV and a neutralino mass of 50 GeV . Finally, limits on two simplified models of dark matter production in association with a $t\bar{t}$ pair are presented as a function of the dark matter particle mass, the mediator mass, and the coupling strength. A pseudoscalar or scalar mediator lighter than 330 GeV is excluded for a coupling strength of 3.5 and a dark matter particle mass below 20 GeV .

References

- [1] F. Zwicky, *Die Rotverschiebung von extragalaktischen Nebeln*, Helv. Phys. Acta **6** (1933) 110.
- [2] G. Bertone, D. Hooper and J. Silk, *Particle dark matter: Evidence, candidates and constraints*, Phys. Rept. **405** (2005) 279, arXiv: [hep-ph/0404175](#).
- [3] G. Jungman, M. Kamionkowski and K. Griest, *Supersymmetric dark matter*, Phys. Rept. **267** (1996) 195, arXiv: [hep-ph/9506380](#) [hep-ph].
- [4] J. Binney and S. Tremaine, *Errata in Binney and Tremaine, 'Galactic Dynamics'*, (1993), arXiv: [astro-ph/9304010](#) [astro-ph].
- [5] Y. Gofland and E. Likhtman, *Extension of the Algebra of Poincare Group Generators and Violation of p Invariance*, JETP Lett. **13** (1971) 323.
- [6] D. Volkov and V. Akulov, *Is the Neutrino a Goldstone Particle?*, Phys. Lett. B **46** (1973) 109.
- [7] J. Wess and B. Zumino, *Supergauge Transformations in Four-Dimensions*, Nucl. Phys. B **70** (1974) 39.
- [8] J. Wess and B. Zumino, *Supergauge Invariant Extension of Quantum Electrodynamics*, Nucl. Phys. B **78** (1974) 1.
- [9] S. Ferrara and B. Zumino, *Supergauge Invariant Yang-Mills Theories*, Nucl. Phys. B **79** (1974) 413.
- [10] A. Salam and J. A. Strathdee, *Supersymmetry and Nonabelian Gauges*, Phys. Lett. B **51** (1974) 353.
- [11] C. Regis et al., *Search for Proton Decay via $p- > \mu^+ K^0$ in Super-Kamiokande I, II, and III*, Phys. Rev. D **86** (2012) 012006, arXiv: [1205.6538](#) [hep-ex].
- [12] G. R. Farrar and P. Fayet, *Phenomenology of the Production, Decay, and Detection of New Hadronic States Associated with Supersymmetry*, Phys. Lett. B **76** (1978) 575.
- [13] P. Fayet, *Supersymmetry and Weak, Electromagnetic and Strong Interactions*, Phys. Lett. B **64** (1976) 159.
- [14] P. Fayet, *Spontaneously Broken Supersymmetric Theories of Weak, Electromagnetic and Strong Interactions*, Phys. Lett. B **69** (1977) 489.
- [15] H. Goldberg, *Constraint on the Photino Mass from Cosmology*, Phys. Rev. Lett. **50** (1983) 1419, [Erratum: Phys. Rev. Lett. **103** (2009) 099905].
- [16] J. R. Ellis et al., *Supersymmetric Relics from the Big Bang*, Nucl. Phys. B **238** (1984) 453.
- [17] G. Steigman and M. S. Turner, *Cosmological Constraints on the Properties of Weakly Interacting Massive Particles*, Nucl. Phys. B **253** (1985) 375.
- [18] ATLAS Collaboration, *Search for dark matter in events with heavy quarks and missing transverse momentum in pp collisions with the ATLAS detector*, Eur. Phys. J. C **75** (2015) 92, arXiv: [1410.4031](#) [hep-ex], EXOT-2014-01.
- [19] *Search for the Production of Dark Matter in Association with Top Quark Pairs in the Single-lepton Final State in pp collisions at $\sqrt{s} = 8$ TeV*, (2014), URL: <https://cds.cern.ch/record/1749153>.

- [20] *Search for New Physics with a Monojet and Missing Transverse Energy in pp Collisions at $\sqrt{s} = 7$ TeV*, (2011), URL: <https://cds.cern.ch/record/1376675>.
- [21] *Search for Dark Matter produced in association with bottom quarks*, (2016), URL: <https://cds.cern.ch/record/2138506>.
- [22] M. Beltran et al., *Maverick dark matter at colliders*, *JHEP* **1009** (2010) 037, arXiv: [1002.4137 \[hep-ph\]](https://arxiv.org/abs/1002.4137).
- [23] P. J. Fox et al., *Missing Energy Signatures of Dark Matter at the LHC*, *Phys. Rev. D* **85** (2012) 056011, arXiv: [1109.4398 \[hep-ph\]](https://arxiv.org/abs/1109.4398).
- [24] J. Goodman et al., *Constraints on Dark Matter from Colliders*, *Phys. Rev. D* **82** (2010) 116010, arXiv: [1008.1783 \[hep-ph\]](https://arxiv.org/abs/1008.1783).
- [25] D. Abercrombie et al., *Dark Matter Benchmark Models for Early LHC Run-2 Searches: Report of the ATLAS/CMS Dark Matter Forum*, (2015), ed. by A. Boveia et al., arXiv: [1507.00966 \[hep-ex\]](https://arxiv.org/abs/1507.00966).
- [26] M. R. Buckley, D. Feld and D. Goncalves, *Scalar Simplified Models for Dark Matter*, *Phys. Rev. D* **91** (2015) 015017, arXiv: [1410.6497 \[hep-ph\]](https://arxiv.org/abs/1410.6497).
- [27] U. Haisch and E. Re, *Simplified dark matter top-quark interactions at the LHC*, *JHEP* **06** (2015) 078, arXiv: [1503.00691 \[hep-ph\]](https://arxiv.org/abs/1503.00691).
- [28] G. Busoni et al., *On the Validity of the Effective Field Theory for Dark Matter Searches at the LHC, Part II: Complete Analysis for the s -channel*, *JCAP* **1406** (2014) 060, arXiv: [1402.1275 \[hep-ph\]](https://arxiv.org/abs/1402.1275).
- [29] G. Busoni et al., *On the Validity of the Effective Field Theory for Dark Matter Searches at the LHC Part III: Analysis for the t -channel*, *JCAP* **1409** (2014) 022, arXiv: [1405.3101 \[hep-ph\]](https://arxiv.org/abs/1405.3101).
- [30] G. Busoni et al., *On the Validity of the Effective Field Theory for Dark Matter Searches at the LHC*, *Phys. Lett. B* **728** (2014) 412, arXiv: [1307.2253 \[hep-ph\]](https://arxiv.org/abs/1307.2253).
- [31] ATLAS Collaboration, *ATLAS Run 1 searches for direct pair production of third-generation squarks at the Large Hadron Collider*, *Eur. Phys. J. C* **75** (2015) 510, arXiv: [1506.08616 \[hep-ex\]](https://arxiv.org/abs/1506.08616).
- [32] M. Aaboud et al., *Search for top squarks in final states with one isolated lepton, jets, and missing transverse momentum in $\sqrt{s} = 13$ TeV pp collisions with the ATLAS detector*, (2016), arXiv: [1606.03903 \[hep-ex\]](https://arxiv.org/abs/1606.03903).
- [33] CMS Collaboration, *Search for top-squark pair production in the single-lepton final state in pp collisions at $\sqrt{s} = 8$ TeV*, *Eur. Phys. J. C* **73** (2013) 2677, arXiv: [1308.1586 \[hep-ex\]](https://arxiv.org/abs/1308.1586), CMS-SUS-13-011.
- [34] CMS Collaboration, *Search for supersymmetry using razor variables in events with b -tagged jets in pp collisions at $\sqrt{s} = 8$ TeV*, *Phys. Rev. D* **91** (2015) 052018, arXiv: [1502.00300 \[hep-ex\]](https://arxiv.org/abs/1502.00300), CMS-SUS-13-004.
- [35] CMS Collaboration, *Searches for supersymmetry using the M_{T2} variable in hadronic events produced in pp collisions at 8 TeV*, *JHEP* **05** (2015) 078, arXiv: [1502.04358 \[hep-ex\]](https://arxiv.org/abs/1502.04358), CMS-SUS-13-019.

[36] CMS Collaboration, *Searches for third-generation squark production in fully hadronic final states in proton–proton collisions at $\sqrt{s} = 8$ TeV*, *JHEP* **06** (2015) 116, arXiv: [1503.08037 \[hep-ex\]](#), CMS-SUS-14-001.

[37] CMS Collaboration, *Search for supersymmetry in events with soft leptons, low jet multiplicity, and missing transverse momentum in proton–proton collisions at $\sqrt{s} = 8$ TeV*, (2015), arXiv: [1512.08002 \[hep-ex\]](#), CMS-SUS-14-021.

[38] CMS Collaboration, *Search for direct pair production of scalar top quarks in the single- and dilepton channels in proton–proton collisions at $\sqrt{s} = 8$ TeV*, *JHEP* (2016), arXiv: [1602.03169 \[hep-ex\]](#), CMS-SUS-14-015.

[39] CMS Collaboration, *Search for new physics with the M_{T2} variable in all-jets final states produced in pp collisions at $\sqrt{s} = 13$ TeV*, (2016), arXiv: [1603.04053 \[hep-ex\]](#), CMS-SUS-15-003.

[40] ATLAS Collaboration, *The ATLAS Experiment at the CERN Large Hadron Collider*, *JINST* **3** (2008) S08003, PERF-2007-01.

[41] ATLAS Collaboration, *ATLAS Insertable B-Layer Technical Design Report*, 2010, URL: <https://cds.cern.ch/record/1291633>.

[42] ATLAS Collaboration, *2015 start-up trigger menu and initial performance assessment of the ATLAS trigger using Run-2 data*, ATL-DAQ-PUB-2016-001, 2016, URL: <https://cds.cern.ch/record/2136007>.

[43] ATLAS Collaboration, *Improved luminosity determination in pp collisions at $\sqrt{s} = 7$ TeV using the ATLAS detector at the LHC*, *Eur. Phys. J. C* **73** (2013) 2518, arXiv: [1302.4393 \[hep-ex\]](#), DAPR-2011-01.

[44] ATLAS Collaboration, *Luminosity determination in pp collisions at $\sqrt{s} = 8$ TeV using the ATLAS detector at the LHC, to be submitted to Eur. Phys. J. C*.

[45] ATLAS Collaboration, *Electron efficiency measurements with the ATLAS detector using the 2012 LHC proton-proton collision data*, ATLAS-CONF-2014-032, 2014, URL: <http://cds.cern.ch/record/1706245>.

[46] ATLAS Collaboration, *Electron identification measurements in ATLAS using $\sqrt{s} = 13$ TeV data with 50 ns bunch spacing*, ATL-PHYS-PUB-2015-041, 2015, URL: <http://cds.cern.ch/record/2048202>.

[47] ATLAS Collaboration, *Muon reconstruction performance in early Run II*, ATL-PHYS-PUB-2015-037, 2015, URL: <http://cds.cern.ch/record/2047831>.

[48] W. Lampl et al., *Calorimeter Clustering Algorithms: Description and Performance*, ATL-LARG-PUB-2008-002, 2008, URL: <http://cdsweb.cern.ch/record/1099735>.

[49] M. Cacciari, G. P. Salam and G. Soyez, *The anti- kt jet clustering algorithm*, *JHEP* **04** (2008) 063, arXiv: [0802.1189 \[hep-ph\]](#).

[50] ATLAS Collaboration, *Jet Calibration and Systematic Uncertainties for Jets Reconstructed in the ATLAS Detector at $\sqrt{s} = 13$ TeV*, ATL-PHYS-PUB-2015-015, 2015, URL: <http://cds.cern.ch/record/2028594>.

[51] ATLAS Collaboration, *Tagging and suppression of pileup jets with the ATLAS detector*, ATLAS-CONF-2014-018, 2014, URL: <http://cdsweb.cern.ch/record/1700870>.

[52] ATLAS Collaboration, *Optimization of the ATLAS b-tagging performance for the 2016 LHC Run*, ATL-PHYS-PUB-2016-012, 2016, URL: <http://cds.cern.ch/record/2160731>.

[53] ATLAS Collaboration, *Performance of b-Jet Identification in the ATLAS Experiment*, JINST **11** (2016) P04008, arXiv: [1512.01094 \[hep-ex\]](https://arxiv.org/abs/1512.01094), PERF-2012-04.

[54] ATLAS Collaboration, *Performance of missing transverse momentum reconstruction for the ATLAS detector in the first proton-proton collisions at $\sqrt{s} = 13$ TeV*, ATL-PHYS-PUB-2015-027, 2015, URL: <http://cds.cern.ch/record/2037904>.

[55] ATLAS Collaboration, *Expected performance of missing transverse momentum reconstruction for the ATLAS detector at $\sqrt{s} = 13$ TeV*, ATL-PHYS-PUB-2015-023, 2015, URL: <http://cds.cern.ch/record/2037700>.

[56] M. R. Buckley et al., *Super-Razor and Searches for Sleptons and Charginos at the LHC*, Phys. Rev. D **89** (2014) 055020, arXiv: [1310.4827 \[hep-ph\]](https://arxiv.org/abs/1310.4827).

[57] C. G. Lester and D. J. Summers, *Measuring masses of semiinvisibly decaying particles pair produced at hadron colliders*, Phys. Lett. B **463** (1999) 99, arXiv: [hep-ph/9906349](https://arxiv.org/abs/hep-ph/9906349).

[58] A. Barr, C. Lester and P. Stephens, *$m(T2)$: The Truth behind the glamour*, J. Phys. G **29** (2003) 2343, arXiv: [hep-ph/0304226](https://arxiv.org/abs/hep-ph/0304226).

[59] W. S. Cho et al., *Measuring superparticle masses at hadron collider using the transverse mass kink*, JHEP **02** (2008) 035, arXiv: [0711.4526 \[hep-ph\]](https://arxiv.org/abs/0711.4526).

[60] M. Burns et al., *Using Subsystem MT2 for Complete Mass Determinations in Decay Chains with Missing Energy at Hadron Colliders*, JHEP **03** (2009) 143, arXiv: [0810.5576 \[hep-ph\]](https://arxiv.org/abs/0810.5576).

[61] T. Melia, *Spin before mass at the LHC*, JHEP **01** (2012) 143, arXiv: [1110.6185 \[hep-ph\]](https://arxiv.org/abs/1110.6185).

[62] ATLAS Collaboration, *The ATLAS Simulation Infrastructure*, Eur. Phys. J. C **70** (2010) 823, arXiv: [1005.4568 \[hep-ex\]](https://arxiv.org/abs/1005.4568), SOFT-2010-01.

[63] S. Agostinelli et al., *GEANT4: A Simulation toolkit*, Nucl.Instrum.Meth.A **506** (2003) 250.

[64] ATLAS Collaboration, *The simulation principle and performance of the ATLAS fast calorimeter simulation FastCaloSim*, ATL-PHYS-PUB-2010-013, 2010, URL: <http://cds.cern.ch/record/1300517>.

[65] T. Gleisberg et al., *Event generation with SHERPA 1.1*, JHEP **02** (2009) 007, arXiv: [0811.4622 \[hep-ph\]](https://arxiv.org/abs/0811.4622).

[66] ATLAS Collaboration, *Multi-Boson Simulation for 13 TeV ATLAS Analyses*, ATL-PHYS-PUB-2016-002, 2016, URL: <https://cds.cern.ch/record/2119986>.

[67] T. Gleisberg and S. Höche, *Comix, a new matrix element generator*, JHEP **12** (2008) 039, arXiv: [0808.3674 \[hep-ph\]](https://arxiv.org/abs/0808.3674).

[68] F. Caccioli, P. Maierhofer and S. Pozzorini, *Scattering Amplitudes with Open Loops*, Phys. Rev. Lett. **108** (2012) 111601, arXiv: [1111.5206 \[hep-ph\]](https://arxiv.org/abs/1111.5206).

[69] S. Schumann and F. Krauss, *A Parton shower algorithm based on Catani-Seymour dipole factorisation*, JHEP **03** (2008) 038, arXiv: [0709.1027 \[hep-ph\]](https://arxiv.org/abs/0709.1027).

[70] S. Höche et al., *QCD matrix elements + parton showers: The NLO case*, *JHEP* **04** (2013) 027, arXiv: [1207.5030 \[hep-ph\]](#).

[71] H.-L. Lai et al., *New parton distributions for collider physics*, *Phys. Rev. D* **82** (2010) 074024, arXiv: [1007.2241 \[hep-ph\]](#).

[72] ATLAS Collaboration, *Simulation of top quark production for the ATLAS experiment at $\sqrt{s} = 13$ TeV*, ATL-PHYS-PUB-2016-004, 2016, URL: <https://cds.cern.ch/record/2120417>.

[73] M. Czakon and A. Mitov, *Top++: A Program for the Calculation of the Top-Pair Cross-Section at Hadron Colliders*, *Comput.Phys.Commun.* **185** (2014) 2930, arXiv: [1112.5675 \[hep-ph\]](#).

[74] ATLAS Collaboration, *Monte Carlo Generators for the Production of a W or Z/ γ^* Boson in Association with Jets at ATLAS in Run 2*, ATL-PHYS-PUB-2016-003, 2016, URL: <https://cds.cern.ch/record/2120133>.

[75] J. Alwall et al., *The automated computation of tree-level and next-to-leading order differential cross sections, and their matching to parton shower simulations*, *JHEP* **07** (2014) 079, arXiv: [1405.0301 \[hep-ph\]](#).

[76] T. Sjöstrand, S. Mrenna and P. Z. Skands, *A Brief Introduction to PYTHIA 8.1*, *Comput. Phys. Commun.* **178** (2008) 852, arXiv: [0710.3820 \[hep-ph\]](#).

[77] ATLAS Collaboration, *Modelling of the $t\bar{t}H$ and $t\bar{t}V$ ($V = W, Z$) processes for $\sqrt{s} = 13$ TeV ATLAS analyses*, ATL-PHYS-PUB-2016-005, 2016, URL: <https://cds.cern.ch/record/2120826>.

[78] ATLAS Collaboration, *ATLAS Pythia8 tunes to 7 TeV data*, ATL-PHYS-PUB-2014-021, 2014, URL: <http://cds.cern.ch/record/1966419>.

[79] R. D. Ball et al., *Parton distributions with LHC data*, *Nucl. Phys. B* **867** (2013) 244, arXiv: [1207.1303 \[hep-ph\]](#).

[80] G. Corcella et al., *HERWIG 6: An Event generator for hadron emission reactions with interfering gluons (including supersymmetric processes)*, *JHEP* **01** (2001) 010, arXiv: [hep-ph/0011363 \[hep-ph\]](#).

[81] J. Pumplin et al., *New generation of parton distributions with uncertainties from global QCD analysis*, *JHEP* **0207** (2002) 012, arXiv: [hep-ph/0201195 \[hep-ph\]](#).

[82] LHC Higgs Cross Section Working Group, *Handbook of LHC Higgs Cross Sections: 2. Differential Distributions*, CERN-2012-002 (CERN, Geneva, 2012), arXiv: [1201.3084 \[hep-ph\]](#).

[83] L. Lönnblad and S. Prestel, *Matching Tree-Level Matrix Elements with Interleaved Showers*, *JHEP* **03** (2012) 019, arXiv: [1109.4829 \[hep-ph\]](#).

[84] W. Beenakker et al., *Stop production at hadron colliders*, *Nucl. Phys. B* **515** (1998) 3, eprint: [hep-ph/9710451](#).

[85] W. Beenakker et al., *Supersymmetric top and bottom squark production at hadron colliders*, *JHEP* **1008** (2010) 098, eprint: [arXiv:1006.4771 \[hep-ph\]](#).

[86] W. Beenakker et al., *Squark and gluino hadroproduction*, *Int.J.Mod.Phys.A* **26** (2011) 2637, arXiv: [1105.1110 \[hep-ph\]](#).

[87] M. Krämer et al., *Supersymmetry production cross sections in pp collisions at $\sqrt{s} = 7$ TeV*, (2012), arXiv: [1206.2892 \[hep-ph\]](#).

[88] L. Lönnblad and S. Prestel, *Merging Multi-leg NLO Matrix Elements with Parton Showers*, *JHEP* **03** (2013) 166, arXiv: [1211.7278 \[hep-ph\]](#).

[89] D. J. Lange, *The EvtGen particle decay simulation package*, *Nucl. Instrum. Meth. A* **462** (2001) 152.

[90] ATLAS Collaboration, *Summary of ATLAS Pythia 8 tunes*, ATLAS-PHYS-PUB-2012-003, 2012, URL: <http://cdsweb.cern.ch/record/1474107>.

[91] A. D. Martin et al., *Parton distributions for the LHC*, *Eur. Phys. J. C* **63** (2009) 189, arXiv: [0901.0002 \[hep-ph\]](#).

[92] M. Baak et al., *HistFitter software framework for statistical data analysis*, *Eur. Phys. J. C* **75** (2015) 153, arXiv: [1410.1280 \[hep-ex\]](#).

[93] ATLAS collaboration, *Measurement of the top quark-pair production cross section with ATLAS in pp collisions at $\sqrt{s} = 7$ TeV*, *Eur. Phys. J. C* **71** (2011) 1577, arXiv: [1012.1792 \[hep-ex\]](#).

[94] ATLAS collaboration, *Measurement of the top quark pair production cross section in pp collisions at $\sqrt{s} = 7$ TeV in dilepton final states with ATLAS*, *Phys. Lett. B* **707** (2012) 459, arXiv: [1108.3699 \[hep-ex\]](#).

[95] ATLAS Collaboration, *Jet Calibration and Systematic Uncertainties for Jets Reconstructed in the ATLAS Detector at $\sqrt{s} = 13$ TeV*, ATLAS-PHYS-PUB-2015-015, 2015, URL: <https://cds.cern.ch/record/2037613>.

[96] ATLAS Collaboration, *Calibration of b -tagging using dileptonic top pair events in a combinatorial likelihood approach with the ATLAS experiment*, ATLAS-CONF-2014-004, 2014, URL: <http://cdsweb.cern.ch/record/1664335>.

[97] ATLAS Collaboration, *Calibration of the performance of b -tagging for c and light-flavour jets in the 2012 ATLAS data*, (2014), URL: <http://cds.cern.ch/record/1741020>.

[98] P. Kant et al., *HatHor for single top-quark production: Updated predictions and uncertainty estimates for single top-quark production in hadronic collisions*, *Comput. Phys. Commun.* **191** (2015) 74, arXiv: [1406.4403 \[hep-ph\]](#).

[99] A. L. Read, *Presentation of search results: The $CL(s)$ technique*, *J. Phys. G* **28** (2002) 2693.

[100] ATLAS Collaboration, *Search for top squark pair production in final states with one isolated lepton, jets, and missing transverse momentum in $\sqrt{s} = 8$ TeV pp collisions with the ATLAS detector*, *JHEP* **11** (2014) 118, arXiv: [1407.0583 \[hep-ex\]](#), SUSY-2013-15.

[101] ATLAS Collaboration, *Search for direct top-squark pair production in final states with two leptons in pp collisions at $\sqrt{s} = 8$ TeV with the ATLAS detector*, *JHEP* **06** (2014) 124, arXiv: [1403.4853 \[hep-ex\]](#), SUSY-2013-19.